arXiv:1407.8452v1 [astro-ph.SR] 29 Jul 2014

resubmitted 25 Nov 2010

The Mass-Loss Return from Evolved Stars to the Large Magellanic Cloud IV: Construction and Validation of a Grid of Models for Oxygen-Rich AGB Stars, Red Supergiants, and Extreme AGB Stars

Benjamin A. Sargent[1], S. Srinivasan[2], M. Meixner[1]

ABSTRACT

To measure the mass loss from dusty oxygen-rich (O-rich) evolved stars in the Large Magellanic Cloud (LMC), we have constructed a grid of models of spherically-symmetric dust shells around stars with constant mass-loss rates using **2D**ust. These models will constitute the O-rich model part of the "Grid of Red supergiant and Asymptotic giant branch star ModelS" (GRAMS). This model grid explores 4 parameters – stellar effective temperature from 2100 K–4700 K; luminosity from 10^3–$10^6 L_\odot$; dust shell inner radii of 3, 7, 11, and 15 R_{star}; and 10.0 μm optical depth from 10^{-4} to 26. From an initial grid of $\sim$1200 **2D**ust models, we create a larger grid of $\sim$69 000 models by scaling to cover the luminosity range required by the data. These models are offered to the public on a website. The matching in color-magnitude diagrams and color-color diagrams to observed O-rich asymptotic giant branch (AGB) and red supergiant (RSG) candidate stars from the SAGE and SAGE-Spec LMC samples and a small sample of OH/IR stars is generally very good. The extreme AGB star candidates from SAGE are more consistent with carbon-rich (C-rich) than O-rich dust composition. Our model grid suggests lower limits to the mid-infrared colors of the dustiest AGB stars for which the chemistry could be O-rich. Finally, the fitting of GRAMS models to SEDs of sources fit by other studies provides additional verification of our grid and anticipates future, more expansive efforts.

Subject headings: circumstellar matter, infrared: stars, stars: asymptotic giant branch

[1]Space Telescope Science Institute, 3700 San Martin Drive, Baltimore, MD 21218, USA; sargent@stsci.edu

[2]Institut d'Astrophysique de Paris, 98 bis, Boulevard Arago, Paris 75014, France

1. Introduction

Near the ends of their lives, low- to intermediate-mass ($\lesssim 8\ M_{\odot}$) stars become asymptotic giant branch (AGB) stars. "Asymptotic giant branch" denotes the set of stars that approach the red giant stars asymptotically from the blue side in color, in color-magnitude diagrams of globular clusters (e.g., see the analysis of M92 by Sandage & Walker 1966). However, AGB stars reach higher luminosities than red giant stars, as revealed by their lower magnitudes than red giants at near-infrared wavelengths (e.g., Nikolaev & Weinberg 2000; Cioni et al. 2000; Blum et al. 2006). In the Hertzsprung-Russell (HR) diagram, AGB stars may span a range of effective temperatures of 2000 to 5000 K, depending upon such factors as stellar mass, metallicity, carbon-to-oxygen abundance ratio, etc. Groenewegen et al. (2009) find AGB stars' effective temperatures to span the range 2500–3800 K. Busso et al. (2007) find carbon-rich AGB stars with effective temperatures as low as 2000 K, while Marigo et al. (2008) predict AGB stars of very low metallicity (Z $\sim$0.0001) can have effective temperatures as high as $\sim$5000 K. AGB stars' luminosities are typically $>10^3 L_{\odot}$ (e.g., Groenewegen et al. 2009).

Stars in the AGB phase expel their own material. Exactly how this mass-loss occurs is debated, but it is believed that radial pulsations lift material above the surface of the star, dust forms from this material, and the radiation pressure of photons from the star pushing on the newly-formed dust grains propels the dust away from the star, dragging the gas with it (Bowen 1988; Fleischer et al. 1991, 1992; Feuchtinger et al. 1993; Hoefner & Dorfi 1997; Hoefner et al. 1998; Winters et al. 1997, 2000; Jeong et al. 2003; Höfner 2009). As a star enters further into its AGB phase, it increases its mass-loss (Ferrarotti & Gail 2006; Srinivasan et al. 2009; Groenewegen et al. 2009). Red supergiant (RSG) stars are massive stars ($> 8\ M_{\odot}$), that similarly eject their own material toward the ends of their lives. This occurs as they evolve away from the Main Sequence and begin core helium burning, before they explode as supernovae (see, e.g., Massey 2003; Verhoelst et al. 2009). As with AGB stars, RSG stars produce dust by a mechanism that is not yet totally understood, but this mechanism may be similar to that proposed for AGBs (Verhoelst et al. 2009). For a wide range of stellar masses, the end of a star's life is characterized by the return of matter back to the interstellar medium (ISM) from which the star formed originally.

The obscuration of much of the rest of our own Galaxy by its own ISM poses difficulties for studying evolved stars' production of dust and its subsequent life-cycle in the Milky Way. For this reason, we turn to other galaxies for studying the life-cycle of dust and other matter. The low average reddening of E(B-V)$\sim$ 0.075 (Schlegel et al. 1998) toward the Large Magellanic Cloud (LMC), its favorable orientation (24°; see Weinberg & Nikolaev 2001), and especially its proximity ($\sim$50kpc; see Feast 1999) ease determination of important

stellar properties, such as luminosity (or, alternatively, absolute magnitudes). This makes the LMC an optimal target for studying the life-cycle of dust in a galaxy. This is the overarching theme for the Surveying the Agents of a Galaxy's Evolution (SAGE) *Spitzer* Space Telescope (Werner et al. 2004) Legacy project (Meixner et al. 2006). The *Spitzer* Infrared Array Camera (IRAC; Fazio et al. 2004) observations conducted as part of the SAGE project found over 6 million stars in the LMC, including thousands of oxygen-rich (O-rich) AGB stars, carbon-rich (C-rich) AGB stars, and extreme AGB stars (Blum et al. 2006; Srinivasan et al. 2009); RSGs (Bonanos et al. 2009); and Young Stellar Objects (Whitney et al. 2008; Gruendl & Chu 2009) in various stages of evolution. By using the infrared emission from dust, we can study the life cycle of matter as it is expelled from evolved stars, stored in the ISM of the LMC, gathered together in star-forming regions, and incorporated into YSOs to form planetary systems around new stars.

Spectral Energy Distributions (SEDs), plots of emitted power versus wavelength, are used to constrain various properties of AGB stars. One means by which AGB properties are constrained by their SEDs is to fit models to the SEDs of individual AGB stars (e.g., van Loon et al. 1999; Groenewegen et al. 2009; Sargent et al. 2010; Srinivasan et al. 2010). Another approach, perhaps better suited to constraining general properties of relatively large samples of these stars, is to compute a grid of models and compare tracks or grids of these models to data in color-magnitude diagrams (CMDs; plots of magnitude versus color) or color-color diagrams (CCDs; plots of one color versus another). For instance, Volk & Kwok (1988) and Marigo et al. (2008) compute radiative transfer models of AGB stars that also take into account the evolution of these stars, and one of the methods by which they evaluate their resultant evolutionary model tracks is to compare them to observed data in CCDs (Volk & Kwok 1988) and CMDs (Marigo et al. 2008). Others more simply use CMDs and CCDs to verify their radiative transfer model tracks or grids (Ivezic & Elitzur 1995; Groenewegen 2006; González-Lópezlira et al. 2010, e.g.,), though Groenewegen (2006) also simulate evolution from the AGB to post-AGB stages. We adopt the approach of constructing a model grid and comparing it to observed data in CMDs and CCDs (e.g., Ivezic & Elitzur 1995; González-Lópezlira et al. 2010), though we do not attempt to model evolution within the AGB stage or from the AGB to the post-AGB stages as others have done. In subsequent papers, we will return to the first approach and fit the SED of each AGB and RSG candidates in the SAGE database individually.

In this paper we present the grid of models we will later use to study the mass loss of those stars in the SAGE sample identified as candidate O-rich AGB stars, extreme AGB stars, and RSG stars. Using the dust properties found to be reasonable to use in radiative transfer (RT) modeling of the SEDs of two O-rich AGB stars by Sargent et al. (2010), we have computed a grid of thousands of **2D**ust (Ueta & Meixner 2003) radiative transfer

models for O-rich evolved stars. **2D**ust computes radiative transfer through an axisymmetric dust envelope surrounding a star. It accomplishes this by dividing the envelope into a finite number of cells and computing the radiative transfer through each cell. In a companion paper, Srinivasan et al. (2010, *in prep*, "Paper V") are creating a similar model grid for C-rich AGB stars. We test our O-rich model grid by comparing in color-magnitude diagrams (CMDs) and color-color diagrams (CCDs) the colors and magnitudes of our models to those of observed O-rich AGB, RSG, and extreme AGB candidates identified in the SAGE sample. In anticipation of the next step of using our model grid to fit the SED of each candidate O-rich AGB, RSG, and extreme AGB in the SAGE sample, we also include sample fits in this paper to stars whose SEDs have been modeled in other studies, as a test of our model grid.

2. Model Grid

In order to model the thousands of oxygen-rich and extreme AGB star candidates and ~ 100 RSG candidates, we have constructed a grid of $\sim 69\,000$ **2D**ust models. For a summary of the model parameters explored in our grid that will be discussed in this section, see Table 1.

2.1. Initial Grid

To create the final grid of 68 600 models, we first created an initial grid of 1225 models, which we discuss in this subsection. The final grid explores a range of values in four parameters that have the greatest effect upon the output model spectra. These four parameters are stellar effective temperature ($T_{\rm eff}$), dust shell inner radius ($R_{\rm min}$), optical depth at 10.0 μm (τ_{10}), and stellar luminosity ($L_{\rm star}$). The first three are true input parameters, as they are required to be chosen before a model can be run (this includes $T_{\rm eff}$, as the choice of this determines which stellar photosphere model is used in the model). These three are inputs for each **2D**ust model in the initial grid, and a range of values for each of them is explored in the initial grid. As will be discussed individually in detail later, we explored 14 values of $T_{\rm eff}$, 4 values of $R_{\rm min}$, and 39 values of τ_{10}. This gives a total of 2184 total possible models in the initial grid, but of these, only 1225 were kept because the rest had the unphysical condition of dust hotter than the dust sublimation temperature at the dust shell inner radius. The last parameter, luminosity, is technically a calculated output parameter (as we discuss later, it is obtained by integrating the input stellar photosphere model over all wavelengths, then using distance to the star to obtain luminosity; dust mass-loss rate is also a calculated

output) from each model. In constructing the final grid of models from the initial grid, *via* scaling relations that are described below, we do, however, explore a range of 56 values of luminosity. As all models in the final grid result from scaling models in the initial grid, all resultant scaled models were acceptable, so this gave a total of $1225 \times 56 = 68\,600$ models in the final grid. The output model spectra and SEDs are then the true outputs of our models. In addition to being sensitive to the four parameters we explore here, the output models are also sensitive to the properties assumed for the dust grains; however, these have already been explored by Sargent et al. (2010). The output spectra are less sensitive to the model parameters besides the grain properties and the four mentioned previously. Each model is computed using the techniques, procedures, and assumptions described by Sargent et al. (2010). Here, we enumerate and briefly discuss each of the various properties that serve as input to the code.

2.1.1. Varied Model Parameters

As noted previously, we explore both stellar photosphere properties and circumstellar dust shell properties in our model grid. Here we summarize how we allowed these to vary.

Stellar Properties

To represent the stellar photosphere emission in each of our models, we use PHOENIX models (Kučinskas et al. 2005, 2006) for stars of subsolar metallicity ($\log(Z/Z_{\rm Sun}) = -0.5$) to match determinations of the metallicity of the LMC ($\rm Z_{LMC} \simeq 0.5 \times Z_{\odot}$; see Dufour et al. 1982; Bernard et al. 2008). PHOENIX models are given in increments of $\log(Z/Z_{\rm Sun})$ of 0.5, so the one we chose was nearest the LMC's metallicity. We use PHOENIX models with stellar effective temperatures, $\rm T_{eff}$, between 2100 K and 4700 K, inclusive, in increments of 200 K. We briefly explored using PHOENIX models over a range of $\log(\rm g/[cm^{*}s^{-2}])$ values from -0.5 to +2.5, but we found that this did not appreciably affect the colors of the output models, so we use PHOENIX models of $\log(\rm g) = -0.5$ only.

To determine the radius of a star for a single model, the mass of the star was assumed to be 1 $M_{\odot}$, as this was the only stellar mass for which PHOENIX stellar photosphere models were available. The effect of varying stellar mass was explored by Kučinskas et al. (2005). They found the optical-to-infrared colors *V*-*I* and *V*-*K* to be most affected by increasing the mass, with the colors becoming bluer by $\sim$0.1 magnitude when mass was increased from 1 $M_{\odot}$ to 5 $M_{\odot}$for a star with $\rm T_{eff} = 3500$ K and $\log(\rm g) = 0.5$. The *B*-*V* and *J*-*K* colors were less affected, and all colors were less affected for hotter stars. As many of the models in our

grid have $T_{eff} < 3500$ K, the optical-to-infrared colors of the naked stellar photospheres could be a few tenths of a magnitude bluer than the 1 $M_{\odot}$ ones whose models we use. Greater realism in modeling stellar photosphere emission will have to await coverage of higher stellar masses in stellar photosphere model grids.

For all models in the initial grid, this constant combination of 1 $M_{\odot}$ and log(g) = -0.5 gives a stellar radius of $\sim 295\, R_{\odot}$ (this follows not from the blackbody law but instead as a direct consequence of $g = Mr^{-2}$). Since PHOENIX models are given in surface flux units, the choice of T_{eff} and log(g) = -0.5 determines the surface flux of the star. The distance to the LMC and the stellar radius then determines the flux density for the stellar photosphere model. From this flux, **2D**ust computes the stellar luminosity. This combination of stellar radius of $\sim 295\, R_{\odot}$ and the stellar photosphere models we use (with a range of T_{eff} between 2100 K and 4700 K), in turn, gives a range of luminosities in the initial grid of 1500–38000 $L_{\odot}$. As we will describe later, for the final grid we explored a range of luminosities between $10^3 L_{\odot}$ and $10^6 L_{\odot}$ using scaling relations on this initial grid.

Shell Properties

One property of the circumstellar dust shells that greatly affects the output models is optical depth at 10 μm, τ_{10}. As τ_{10} increases, the infrared excess increases. This is expected from analytical arguments (see Eq. 2 of Groenewegen 2006). Our O-rich AGB, RSG, and extreme AGB sample spans a range from barely any excess above stellar photosphere emission to very large infrared excesses; therefore we allowed τ_{10} for our models to range from 10^{-4} to 26.

The other property that had considerable effect on the output models was dust shell inner radius, R_{min}. This parameter determines the temperature of the hottest dust, which, in turn, determines the wavelength in the SED at which the emission from the dust shell becomes significant compared to that of the stellar photosphere. The values of R_{min} explored in our grid were 3, 7, 11, and 15 $\times\, R_{star}$. We chose this range of R_{min} to correspond roughly to the allowable range of dust shell inner radii for O-rich AGB stars (2.5-14 R_{star}) according to Höfner (2007). Note that the dust shell inner radii used by van Loon et al. (1999) in modeling M stars are distributed over this range, and even in some cases approach 14 R_{star}. The temperature of the hottest dust for a given model was allowed to be at most 1400 K, as this is approximately the sublimation temperature of the astrophysically relevant silicates forsterite and enstatite (Posch et al. 2007). We note that we do not have a model for every possible combination of T_{eff}, luminosity, τ_{10}, and R_{min}, as models with their hottest dust higher than 1400 K were rejected from our model grid.

2.1.2. Fixed Properties

Here we summarize those model parameters that are set at fixed values. Since we intend to keep the models as simple as possible, we explore only the model parameters to which the output spectra are most sensitive – stellar effective temperature, stellar luminosity, dust shell optical depth, and dust shell inner radius. We fix the rest of the parameters. This includes those parameters relating to dust grain properties, which for this oxygen-rich model grid are exactly those used by Sargent et al. (2010). This also includes parameters relating to the dust shell geometry, as we assume for simplicity spherically-symmetric dust shells and constant mass-loss rate (again, see Sargent et al. 2010).

Dust Grains

The models are sensitive to the choice of dust grain properties assumed. These dust grain properties were explored by Sargent et al. (2010), so we do not explore changing the dust properties here. Instead, we briefly summarize the findings by Sargent et al. (2010). As a starting point for modeling the mass loss of evolved stars in the LMC, the SEDs of two O-rich AGBs have been modeled (Sargent et al. 2010). From the "faint" population identified by Blum et al. (2006), SSTISAGE1C J052206.92-715017.6 (hereafter, SSTSAGE052206) was chosen, and from the brighter population, HV 5715 was chosen. Using **2D**ust (Ueta & Meixner 2003), RT models were constructed to fit the optical (U through I), near-infrared (J through L), IRAC, and Multiband Imaging Photometer for *Spitzer* (MIPS; Rieke et al. 2004) broadband photometry and *Spitzer* Infrared Spectrograph (IRS; Houck et al. 2004) spectra (5–37 μm wavelength) in the spectral energy distribution (SED) of each of these sources. From this modeling, it was found that the complex indices of refraction of oxygen-deficient silicates from Ossenkopf et al. (1992) provided reasonable fits to both the overall photometry over all wavelengths probed and to the detailed IRS spectrum showing the silicate emission features at $\sim$10 and $\sim$20 μm. The size distribution of these grains was assumed to be a KMH-like "Power-law with Exponential Decay (PED)" (Kim et al. 1994) distribution; that is, the number of grains of radius a, n(a), is proportional to $a^{\gamma}\mathrm{e}^{-a/a_0}$, with γ equal to -3.5, a_{min} of 0.01 μm, and a_0 of 0.1 μm. The models fit the data well, so we assume the dust properties used by Sargent et al. (2010) for the dust in the shells in our model grid. Mie theory is used to compute the absorption cross-sections of the grains. These cross-sections are averaged with Harrington averaging (Harrington et al. 1988) mode (for a description, see Sargent et al. 2010). These average cross-sections are then used in the **2D**ust radiative transfer calculations. We assume isotropic scattering of radiation by the dust grains.

Circumstellar Shell

Spherically-symmetric mass-loss constant over time is assumed for our models, which means the density distribution of dust between the inner radius (R_{min}) and outer radius (R_{max}) goes as $1/R^2$. For each model, R_{max} is set to be $1000 \times R_{min}$. The dust expansion velocity, v_{exp}, for the dust shells is set at 10 km/s, and the distance assumed for our evolved star models is 50kpc (for more, see Sargent et al. 2010).

2.2. Expansion to the Full Grid

The highest luminosity in our initial grid, $\sim 38000 L_{\odot}$, is lower than most of the proposed lower limits on luminosity for a red supergiant (see discussion on HV 5715 by Sargent et al. 2010). To model RSGs and the AGB stars of higher luminosity than allowed by our initial grid, we use scaling relations on this grid. For each model in the final grid, the scalar to be used is determined by dividing the luminosity of the model in the final grid by the luminosity of the model to be scaled from the initial grid. We then multiply the output flux density at all wavelengths for the appropriate model from the initial grid by this scalar (Groenewegen 2006). The radius of the star in the final grid is then determined by multiplying the stellar radius of the model in the initial grid by the square root of the scalar because $L = 4\pi R^2 \sigma T^4$, and T does not change. Further, the dust (and, therefore, total) mass-loss rate of the star is also scaled by the square root of the scalar (this follows from Eq. 2 of Groenewegen 2006). The other model parameters and outputs of concern do not change during this scaling. The new grid has 41 values of luminosity between $10^3 L_{\odot}$ and $2 \times 10^4 L_{\odot}$, inclusive, with equal logarithmic spacing in luminosity, such that consecutive luminosity values differ by a factor of about 1.08. The new grid also has 16 values of luminosity between $2 \times 10^4 L_{\odot}$ and $10^6 L_{\odot}$, inclusive, with equal logarithmic spacing in luminosity, such that consecutive luminosity values differ by a factor of about 1.3. This gives a total of 41 + 15 = 56 unique luminosity values in the new grid.

2.3. Dust Mass-Loss Rate versus Luminosity

In Figure 1 we plot dust mass-loss rate versus luminosity for the grid models that we plot in Figure 6. Here we show both the initial grid (blue points) and final grid (black points), though in all the following figures we only show the final grid. This illustrates the range of luminosities and dust mass-loss rates probed by our models. The luminosities, as noted previously, range from 10^3 to 10^6 $L_{\odot}$. At the lowest luminosities, the dust mass-loss rates

probed is $3.0\times10^{-13}M_{\odot}yr^{-1}$ to $1.0\times10^{-6}M_{\odot}yr^{-1}$. At the highest luminosities, this range is $1.0\times10^{-11}M_{\odot}yr^{-1}$ to $3.0\times10^{-5}M_{\odot}yr^{-1}$.

As we noted previously, we designed our grid to explore AGB star and dust shell parameters over large ranges of values, to be safe in allowing for modeling of anomalous, outlying stars in our sample. In determining the mass return from evolved stars in the LMC, we are interested in the dust mass loss from stars of all mass-loss rates. We note the spread in dust mass-loss rates in our model grid spans a range slightly larger than the range inferred from observations of AGB, RSG and red giant stars and predicted by theory for these stars. At high dust mass-loss rates, our grid borders the dust mass-loss rate of $\sim2.6\times10^{-5}M_{\odot}yr^{-1}$ at the luminosity of $2.2\times10^{5}L_{\odot}$ inferred by Boyer et al. (2010) for the RSG star IRAS 05280-6910. At low dust mass-loss rates, our grid explores slightly lower values than those inferred from predictions by Gail et al. (2009) for early AGB (EAGB) stars. The models of Gail et al. (2009) suggest the lowest total mass-loss rates for EAGB stars to be a few times $10^{-10}\,M_{\odot}$, so, assuming a gas-to-dust mass ratio of a few hundred (e.g., see Srinivasan et al. 2009; Sargent et al. 2010), this implies dust mass-loss rates for EAGB stars of $\sim10^{-12}\,M_{\odot}$. In support of the EAGB modeling by Gail et al. (2009), these authors also predict total mass-loss rates for red giant stars similar to those for EAGB stars. Again assuming a gas-to-dust mass ratio of a few hundred, one may infer the lowest dust mass-loss rates for red giant stars to be similar to those Gail et al. (2009) predict for EAGB stars, $\sim10^{-12}\,M_{\odot}$. This is consistent with the lowest dust mass-loss rates inferred from observations of red giant stars in the globular cluster ω Centauri by McDonald et al. (2009).

3. Computing the Grid

A handful of test models was run on a MacBook Pro laptop computer with a 2.4 GHz Intel Core 2 Duo processor, 4 GB 667 MHz DDR2 SDRAM memory, and Mac OS X version 10.5.8 operating system. These initial models determined useful values of model parameters like MXSTEP and VSPACE (see Ueta & Meixner 2003) that affect the performance and quality of the models[1]. The parameter VSPACE must be as large as possible so that the integration step size for a radiative transfer calculation along a path is as small as possible (smaller than the local mean free path of photons); otherwise, the radiative transfer in the models will not be valid. However, if VSPACE is too large, MXSTEP must increase to allow for a large number of very small steps in radiative transfer calculations. The amount of virtual memory required for a model increases as MXSTEP increases, so it is good if MXSTEP is not

[1]see also the User's Manual at http://www.stsci.edu/science/2dust/reference.cgi

too large. The amount of virtual memory allowed for a single model calculation is just over 2 GB. As we had a wide range of optical depths, we took a piecewise approach to the values of VSPACE/MXSTEP we used. For different ranges of optical depth we chose different combinations of VSPACE and MXSTEP. We verified for our models that the requirements were met of not only maximum integration step size (as set by VSPACE) not exceeding the local photon mean free path but also the maximum number of steps along a path not exceeding MXSTEP.

The models for our initial grid were run on the Royal Linux computing cluster at the Space Telescope Science Institute (STScI). The cluster consists of 23 computing nodes, each with 2×2×2.4 GHz processors, 8 GB RAM, 160 GB local disk space, and 17 TB of total disk space. Royal enables up to 88 jobs to be computed simultaneously at high computing speeds and automates the scheduling of computing jobs. Scripts written by the user enable the hundreds or thousands of models in the grid to be submitted for scheduling automatically, minimizing the amount of user intervention required to begin the computing of the grid. Only the initial grid needed to be computed with Royal, as scaling required that no additional **2D**ust models to be run, only that existing **2D**ust models be scaled. **2D**ust on Royal was run in non-interactive mode for these models, as it would not be able to run automatically in interactive mode on the Royal cluster. The number of radial grid points, NRAD, in the model shells was set to 45, and the number of azimuthal grid points, NQ, in the model shells was set to 6.

It would be too time-consuming to try to run all the models desired serially on a single computer. Though we ran a few test case models on a laptop computer, we made use of the Royal Linux computing cluster at Space Telescope Science Institute (STScI) to finish computation of our model grid in a reasonable amount of time. Our initial grid had 4 values of $R_{\rm min}$, 14 values of T_{eff}, and 39 values of τ_{10}, for a grand total of 2 184 models computed in our initial grid. The Royal cluster can work on 88 different computing jobs separately at a given time. For all models with $\tau_{10} < 1$, the computation time per model was about 5 minutes, so the total processing time (the total time it would take to compute all models if only one model could be run at a time) was about 4×14×13×(5 min) = 60.7 hours. Assuming 88 models could be computed simultaneously, this amounted to about 0.7 hours wall time (the total time elapsed while models were running, assuming 88 at a time, from when the first model began to when the last model finished). For models with intermediate values of τ_{10} of 1–10, the computation time per model was about 1 hour. So for all models of τ_{10} between 1 and 10, the total processor time was about 4×14×10×(1 hour) = 560 hours, while the total wall time (again assuming 88 models could be computed at a time) was $\sim$6.4 hours. For the rest of the models (those with τ_{10} between 11 and 26, the computation time per model was on average about 2 hours. For all these, the total processor time was

4×14×16×(2 hours) = 896 hours, while the total wall time was ∼10.2 hours. Altogether, the total processor time was ∼1500 hours, while the total wall time was about 0.7+6.4+10.2 = 17.3 hours. Of the 2 184 models that were computed in the initial grid, 1225 (∼56%) of them were kept and the others rejected because the dust temperature at R_{min} was higher than 1400 K. This initial grid was scaled to arrive at a final grid of 68 600 models.

We call our model grid, to which we will add models for C-rich AGB stars (Srinivasan et al, *in prep*), the "Grid of Red supergiant and Asymptotic giant branch star ModelS" (GRAMS). We offer our final model grid to the public on a publicly-accessible website[2]. Users can download the model **2D** spectra and files containing the input parameters and output values of interest, including dust mass-loss rate, dust temperature at dust shell inner radius, and the parameters listed in Table 1. In addition, photometry synthesized from our **2D**ust models are also available on the website. For details on the synthesis of these fluxes, see Sargent et al. (2010). Such synthesized fluxes can be transformed to magnitudes and compared to observed data on color-magnitude diagrams and color-color diagrams, as we do in the following section.

4. Discussion

We test the general usefulness of our model grid by comparing, in color-magnitude diagrams (CMDs) and color-color diagrams (CCDs), photometry synthesized from our grid to that observed for various evolved stars. These evolved stars include SAGE sample candidate O-rich and extreme AGB stars and RSGs and O-rich AGB stars and RSGs in the SAGE-Spec sample. Although the C-rich AGB stars are being modeled by Srinivasan et al. (2010, *in prep*; "Paper V"), we include the C-rich AGB star sample from SAGE and SAGE-Spec to determine how well the models differentiate between the types, especially for the extreme AGB stars. We identify the O-rich, C-rich, and extreme AGB star samples from SAGE that we include in our analyses by using the criteria given by Srinivasan et al. (2009). We include RSGs from the SAGE sample as identified by Bonanos et al. (2009). Also, we include O-rich AGB stars, RSGs, and C-rich AGB stars from SAGE-Spec that were identified as such by Woods et al. (2010), using *Spitzer*-IRS spectra and ancillary photometry. For the SAGE-Spec sample, a star was only included here if it had a full 5–37 μm spectrum (as opposed to a 5–14 μm spectrum only), in order that its dust chemistry be highly constrained. Some of the O-rich and C-rich AGB stars from SAGE-Spec are quite dusty and provide useful guidance in identifying the dust chemistry for the extreme AGB stars. From SAGE-Spec,

[2]see http://www.stsci.edu/science/2dust/grams_models.cgi

in total we include 34 O-rich AGB stars, 18 RSGs, and 47 C-rich AGB stars. Additionally, we found SAGE photometry for the 10 OH/IR stars detected in OH maser emission by Marshall et al. (2004) and listed in their Table 2. These OH/IR stars have properties (i.e., colors and magnitudes) that we might expect for O-rich extreme AGB stars. As such, these stars represent an advanced stage of mass-loss by O-rich evolved stars, and so they allow us to evaluate our optically thicker O-rich models. We applied zero-point offsets to 2MASS data (as recommended by Cohen et al. 2003). Note that we do not attempt to match our model grid for O-rich evolved stars to observed C-rich AGB stars and candidates. A model grid for C-rich AGB stars is being computed in order to match observed data for C-rich AGB stars and candidates (Paper V).

We must caution that, though these comparisons between grid models and data in CMDs and CCDs show consistency between our model grid as a whole and observed data, one must be careful not to draw too many conclusions from these model/data comparisons in CMDs and CCDs. Though we have made an effort to avoid unrealistic models (e.g., no models with dust temperature at dust shell inner radius greater than dust sublimation temprtature, dust shell inner radius in the range expected by theory, etc.), certain combinations of model $T_{\rm eff}$, $R_{\rm min}$, τ_{10}, and $L_{\rm star}$ may be unlikely or even unphysical. However, we wish to cover a somewhat larger range of the parameters varied in our grid than expected.

4.1. CMD and CCD Comparisons of Model Grid to Data

4.1.1. Color-Magnitude Diagrams

Color-magnitude diagrams are more useful in separating populations of sources with different luminosities. We use this to our advantage here to draw the RSG candidate population away from the O-rich AGB candidate population and evaluate how our model grid covers each population, in addition to the extreme AGB candidate population. Our model grid is consistent with almost all of the observed data in the CMDs for O-rich AGB star candidates from the SAGE sample, the O-rich AGB stars from SAGE-Spec, RSG star candidates from SAGE, RSG stars from SAGE-Spec, the OH/IR stars from Marshall et al. (2004), and the extreme AGB candidates from SAGE.

K_s versus J-K_s

The K_s versus J-K_s CMD is quite useful to discuss, as we use it in identification of O- and C-rich AGBs in the SAGE sample (see discussion in Section 2.1). Figure 2 shows the objects

identified as candidate O-rich AGB stars, C-rich AGB stars, RSGs, and extreme AGB stars in the SAGE sample plotted as blue, purple, red, and green points, respectively. The O-rich AGB candidates form a nearly vertical column of slightly positive slope, with the density of points decreasing to lower K_s magnitudes. At $K_s \lesssim 9$, the RSG candidates form a column approximately parallel to but offset from the O-rich AGB candidates. At the same range of K_s magnitudes but with slightly redder J-K_s colors are the C-rich AGB stars. Toward redder J-K_s colors than the C-rich AGB candidates but at similar K_s magnitudes to them are the extreme AGB candidates. Also plotted are points corresponding to our model grid, as small black points. We note that the black points line up roughly in columns, corresponding to sets of models with the same T_{eff}, R_{min}, and τ_{10} but different luminosity.

Our models reproduce the range of near-infrared colors and magnitudes observed in the SAGE and SAGE-Spec samples quite well. All 17 956 O-rich AGB candidates identified from SAGE photometry as well as the 32 AGB stars whose O-rich chemistries have been confirmed from SAGE-Spec spectra fall within the coverage of our models. We have finer luminosity resolution in the range 10^3 to $2\times10^4 L_\odot$ by design, corresponding to the greatest concentration of O-rich AGB candidate points (for $K_s \gtrsim 9.5$). This is in anticipation of future efforts to model the SED of each O-rich AGB star candidate in detail, with the intention to constrain accurately the luminosity of each candidate O-rich AGB star. Further, the points plotted as small gold stars, identified as O-rich AGB stars in the SAGE-Spec sample (Woods et al. 2010), are also well-matched by the model grid, with the exception of three points at (J-K_s, K_s) of (1.46, 9.36), (1.90, 10.41), and (2.04, 12.90). These three points belong to MSX LMC 61, SSTISAGE1C J053128.42-701027.2, and SSTISAGE1C J045128.56-695550.1, respectively, all of which have SAGE-Spec spectra showing emission features at 10 and 20 μm wavelength belonging to silicates, confirming their O-rich natures. This mixing of O-rich AGB stars in this CMD in the region of moderately red colors dominated by C-rich AGB stars has been noted before (Marigo et al. 2008). The brown triangles, representing the OH/IR stars from Marshall et al. (2004), are also all covered by our model grid. These 8 OH/IR stars lie at redder colors than the vast majority of the O-rich AGB stars and RSG stars, and, with the exception of IRAS 05280-6910, they have $K_s \lesssim 10.5$. IRAS 05280-6910, located at about (1.5, 12.8), is somewhat isolated from other O-rich stars but is near the SAGE-Spec O-rich AGB star SSTISAGE1C J045128.56-695550.1. Two of the 10 OH/IR stars from Marshall et al. (2004) have no J magnitudes in the SAGE catalog and are not plotted. The magenta star symbols are C-rich AGB stars from the SAGE-Spec sample, which, like the C-rich AGB stars from SAGE, should not be expected to be covered by our O-rich grid.

The model grid covers 107 of the 108 RSG stars in the SAGE sample and all 18 RSGs in the SAGE-Spec sample. The one SAGE RSG star not covered by the grid has a J-K_s

color only $\sim$0.01 magnitude less than the bluest models in the grid. According to Skrutskie et al. (2006), the 1-σ uncertainty for this point, which lies near (J-K_s, K_s) = (0.6, 7.8), in K_s is $\sim$0.01 magnitude for K_s = 7.8, and the uncertainty in J is $\sim$0.015 magnitude for J = 8.4. The 3-σ uncertainty in the J-K_s color is then $\sim$0.05, so this uncovered RSG star from SAGE is consistent with the model grid. The RSG candidates in the SAGE-Spec sample, plotted as filled small orange circles, land on top of the densest concentration of SAGE RSG candidate points and are fully covered by the grid, further confirming the good coverage of the RSGs by our model grid. Our grid also covers almost all of the extreme AGB star candidates (1123/1125). Only two are outside of the range of our model grid, but we note that extending the grid to lower luminosities would allow these two points to be covered by our grid. However, as the majority of extreme AGB stars shown in this CMD may not have O-rich dust chemistry (see later discussion), it may be of little meaning that lower luminosity models would cover these two points. In the future, we hope to use SED-fitting as a means to distinguish O-rich from C-rich dust chemistry among the extreme AGB sample.

[8.0] versus [3.6]-[8.0]

Qualitatively, this one is similar to the K_s versus J-K_s CMD discussed previously. The O-rich AGB candidates are faintest and bluest in color, while the RSG candidates have similar color but are brighter. The C-rich AGB star candidates have brightnesses similar to the O-rich AGB candidates but have redder colors, while the extreme AGB star candidates are somewhat brighter and much redder. We note the O-rich AGB candidate points now form a "wedge", the pointed end of which is at the bluest colors and highest magnitudes, and opposite end of which extends toward red colors and the lowest magnitudes. There is a slight overlap between the brightest O-rich AGB candidate points in this "wedge" and the redder RSG candidates. We note, however, moderate overlap between the O-rich AGB and extreme AGB candidates in the SAGE sample around [3.6]-[8.0] $\sim$0.5 and [8.0] $\sim$9. Here, the extreme AGB candidates' [8.0] magnitudes appear to be similar to the brightest [8.0] magnitudes of the O-rich AGB candidate stars. Again we note the overlap between RSG and O-rich AGB candidates for the reddest colors. The isolated O-rich AGB star from SAGE-Spec at ([3.6]-[8.0],[8.0]) of (2.39, 5.08) is IRAS 05298-6957. This star is also in the Marshall et al. (2004) OH/IR list and so is plotted here as a brown triangle. It has silicate absorption features and is therefore confirmed to have O-rich dust. The data point for this star on this CMD is in the same location as the region in the same CMD shown by Matsuura et al. (2009) occupied by a handful of spectroscopically-confirmed O-rich AGB or RSG stars intruding into the region dominated by C-rich AGB stars.

Again, the model grid is very successful in matching the regions spanned by the O-rich

AGB star candidates (from both SAGE and SAGE-Spec samples), RSG candidates (SAGE and SAGE-Spec), and extreme AGB candidates. The O-rich AGB candidates from SAGE with the bluest [3.6]-[8.0] colors are missed by the model grid, as only 9507 out of 17783 of these are directly covered by the model grid. However, of the 8276 that are not directly covered by the model grid, all but 2 of these are consistent within 3σ errors with the model grid. The 1σ error for stars of [3.6] $\sim$12 in the IRAC 3.6 μm band in SAGE Epoch 1 is $\sim$0.1 magnitude[3], and [3.6]-[8.0] $\sim$ 0 for these, so the 3σ error in the [3.6]-[8.0] color would be $\sim$0.4. There are about 6 O-rich AGB candidates in the SAGE sample with colors bluer than -0.3 (approximately the bluest color on this CMD that could be consistent with the model grid), but there are also 2 C-rich AGB candidates with similarly blue colors, so these 6 O-rich AGB candidates in SAGE may be misidentified. The model grid covers 32 out of 34 O-rich AGB stars from SAGE-Spec, 103 out of 109 RSGs from the SAGE sample, and 16 out of 18 RSGs from the SAGE-Spec sample. The few RSGs from SAGE and SAGE-Spec not covered by the model grid have [8.0]$\sim$ 9 and zero [3.6]-[8.0] color, so they have [3.6]$\sim$ 9 as well. At these magnitudes, the 1σ errors on the [3.6] and [8.0] magnitudes should be about 0.05 and 0.03 magnitudes, respectively, so the 3σ error on the [3.6]-[8.0] color for the SAGE and SAGE-Spec RSGs could be up to 0.17 magnitude. Similarly, the two SAGE-Spec O-rich AGB stars have [8.0] $\sim$ [3.6] $\sim$ 10. For these, the typical uncertainties on the [3.6]-[8.0] color would be slightly higher. The 2 O-rich AGB stars and 2 RSG stars from SAGE-Spec and the 6 RSGs from SAGE not directly covered by the grid are therefore still consistent with the model grid.

All 10 of the OH/IR stars from Marshall et al. (2004) are covered by the grid. Most of these cluster around ([3.6]-[8.0],[8.0]) = (2, 6), while the one near (5,4.5) is IRAS 05280-6910, and the one near (2.4, 2.7) is IRAS 04553-6825 (WOH G64). In the SAGE sample, 1411 out of 1427 extreme AGB star candidates are covered by the model grid in this CMD. Those that are not are redder than the reddest models in the grid. These extreme AGB candidates fall in the same region of this CMD as C-rich AGBs from the SAGE-Spec sample, which suggests these reddest extreme AGB star candidates on this CMD have carbon-rich dust. Further, this suggests our grid of O-rich models should not be expected to match the reddest extreme AGB candidates on this plot.

[24] versus [8.0]-[24]

The [24] versus [8.0]-[24] CMD, plotted in Figure 4, differs from the rest of the CMDs we have discussed. Here we see the O-rich AGB candidates branch into two arms at the reddest

[3]see http://irsa.ipac.caltech.edu/data/SPITZER/SAGE/doc/SAGEDataDescription_Delivery2.pdf

[8.0]-[24] colors, a brighter population and a fainter population. The fainter population was identified as "F" in the same CMD shown by Blum et al. (2006). The RSG candidates extend from the brighter arm. The extreme AGB candidates, however, now appear brighter than both the O-rich AGB candidates and the RSG candidates. The mid-IR fluxes of xAGB stars are dominated by contribution from circumstellar dust, and their SEDs hence peak at longer wavelengths than those of optically thin O-rich AGB stars or RSG stars. Again, the isolated O-rich AGB star from the SAGE-Spec sample at ([8.0]-[24],[24]) of (3.00, 2.09) is IRAS 05298-6957 (again, also from the OH/IR list of Marshall et al. 2004), confirmed to have O-rich dust, and it is also plotted here as a brown triangle.

We include in Figure 4 four tracks with points plotted on them. Each track represents a set of models for which all parameters are the same except for τ_{10}, which is allowed to vary. The effect of varying τ_{10} is demonstrated within each track. Each yellow circle on a track is for a different value of τ_{10}, with the lowest values (optically thin models) being at the bluest colors and highest values (optically thick models) being at the reddest colors. These tracks show that varying τ_{10} has a large effect upon the [8.0]-[24] color. These tracks are not evolutionary models; instead, they demonstrate the effect of chaning the various parameters on the colors and magnitudes of the models. Ivezic & Elitzur (1995) performed a similar exercise, with IRAS color-color diagrams instead of the CMD we explore here, to explore varying the optical depth of their dust shell models on model colors. From bottom (greatest [24] magnitude) to top (lowest [24] magnitude), the tracks are for models with the following combinations of $T_{\rm eff}$, $R_{\rm min}$, and luminosity: 2100 K, 15 R_{star}, and 4820$L_{\odot}$; 3700 K, 15 R_{star}, and 16000$L_{\odot}$; 2100 K, 7 R_{star}, and 57000$L_{\odot}$; and finally 2700 K, 7 R_{star}, and 124000$L_{\odot}$.

$T_{\rm eff}$ has an effect like that of optical depth but lesser in strength. Namely, cooler stars give rise to the reddest models for the optically thickest sources (bottommost track), while warmer stars give rise to the bluest models for the optically thinnest sources (the track that is second from bottom). Changing the luminosity translates a track vertically without distortion, as the flux at each wavelength in a model is scaled by the same scalar to generate a new model with all parameters the same except for the new luminosity (equal to the old luminosity multiplied by the aforementioned scalar). This exact effect is not shown, but note that, from bottom to top, the tracks correspond to increasing values of luminosity. The slope of each track changes around the range of [8.0]-[24] colors of 2–4. This inflection is most likely due to the flattening of the model SED at mid-infrared wavelengths ($\sim 10\,\mu$m) due to the dust shell becoming optically thick at these wavelengths and also the 10 μm silicate feature transforming from being in emission for $\tau_{10} < 1$ to absorption when $\tau_{10} > 1$. The effect of varying $R_{\rm min}$ is demonstrated by the lowest and second-highest tracks. For these two tracks, $T_{\rm eff}$ is the same, but the dust shell inner radius is 15 R_{star} for the lower one and 7 R_{star} for the higher one. For dust shells of $\tau_{10} = 1$ (indicated for a given track by a yellow

circle with a red X overlaid), the dust shell with $R_{min} = 7\,R_{star}$ has hotter dust overall; therefore, it lies at a bluer color than the one with $R_{min} = 15\,R_{star}$ and $\tau_{10} = 1$.

The coverage of O-rich AGB candidates, RSG candidates, and extreme AGB candidates by the model grid for this CMD is similar in quality to that for the previous one, [8.0] versus [3.6]-[8.0]. Most of the three populations are covered by the model grid, except for stars with the bluest and reddest [8.0]-[24] colors and largest [24] magnitudes. At bluer colors than the blue edge of the model grid coverage lie 186 out of the 5564 O-rich AGB star candidates from SAGE, 3 out of 105 RSG candidates from SAGE, and 28 of the 1352 SAGE extreme AGB star candidates. At [24]$\sim$ 11, the 1σ error in [24] is >0.2, probably up to 0.5 magnitudes; for [8.0]-[24] colors around -0.4, [8.0] is about 10.6, and the 1σ error is about 0.05 (again, see the SAGE Data Delivery document). The 3σ error on the [8.0]-[24] color for the faint O-rich AGB SAGE candidates bluer than the model grid could therefore be up to 1.5 magnitudes, so the model grid is consistent with all these candidates. For [24] = 8.5 and [8.0]-[24] = 0, the 3σ error on [8.0]-[24] could be up to 0.2 magnitudes. Thus, the model grid is consistent with all extreme AGB candidates except 1 and all SAGE RSG stars. Note that this does not mean the extreme AGB candidates predominantly have O-rich dust. In fact, our later discussion suggests the opposite, that the extreme AGB stars predominantly have C-rich chemistry, including the extreme AGB candidate that is too blue in color to be consistent with our O-rich grid (see discussion in previous subsection on the [8.0] versus [3.6]-[8.0] CMD regarding the bluest observed points). Beyond the reddest models, there are 9 extreme AGB candidates and 1 O-rich AGB candidate from SAGE. The O-rich AGB candidate suggests that some of the 9 extreme AGB candidates may have oxygen-rich dust chemistry (in which case τ_{10} would be greater than 26), but the presence of 2 C-rich AGB stars from the SAGE-Spec sample in this region of the CMD and the presence of C-rich AGB stars from SAGE-Spec in the same region of the previous CMD suggests the dominant dust chemistry for extreme AGB candidates of these red colors to be carbon-rich. All 34 O-rich AGB stars from SAGE-Spec and all 17 RSG stars from SAGE-Spec are within the model grid coverage. The 8 OH/IR stars from Marshall et al. (2004) are all covered by the grid and are located near (3, 3). A handful of about 10 O-rich AGB star candidates from the SAGE sample with $2 <$ [8.0]-[24] < 4 and $6 <$ [24] < 10 lie at fainter [24] than is covered by the model grid. These likely belong to a third population of either red giant branch (RGB) stars fainter than the tip of the RGB or O-rich AGB stars that have sufficiently low mass that they will not become C-rich AGB stars in the future. Were our model to extend to luminosities lower than $10^3 L_{\odot}$, it could cover these.

4.1.2. Color-Color Diagrams

Color-color diagrams, also known as two-color diagrams, are useful in identifying populations of sources with distinctive changes in broadband colors over a wide wavelength range in an SED. The two colors trace this change in color with wavelength. Again, our model grid is consistent with almost all of the observed data for O-rich AGB star candidates from the SAGE sample, the O-rich AGB stars from SAGE-Spec, RSG star candidates from SAGE, the RSG stars from SAGE-Spec, and the OH/IR stars from Marshall et al. (2004). The extreme AGB candidates from SAGE, however, are frequently not consistent with our model grid in the CCDs, which has implications for the dust chemistry of the extreme AGB candidates.

[5.8]-[8.0] versus [3.6]-[4.5]

This color-color diagram, plotted in Figure 5, traces the change in color over the near-infrared wavelength range of 3–8 μm spanned by the *Spitzer* IRAC bands. The most obvious feature of this CCD is that, in general, the redder a source is in one color, the redder it is in the other. This is due to both colors measuring the same general component - the emission from the circumstellar dust shell. The next most obvious characteristic of this plot is that those sources identified as extreme AGB candidates are generally redder in both colors than both the O-rich AGB and RSG candidates. This suggests that the extreme AGB candidates generally have more dust in their dust shells than either the O-rich AGB or RSG candidates. Additionally, the O-rich AGB and RSG candidates overlap greatly in the plot. This suggests the shell properties or dust properties (or both) are similar between the two populations, and that the more significant difference between the two is their luminosities (see previous discussion on RSG and O-rich AGB candidates in the CMDs).

Here, the coverage of the observed data by the model grid is quite interesting. At the bluest colors, the model grid begins in the middle of the densest concentration of O-rich AGB candidate points at the bluest colors and also close to the bluest RSG candidates. The model grid then extends in the direction of the reddest O-rich AGB candidates (as the O-rich AGB stars in SAGE-Spec and the RSGs from both the SAGE and SAGE-Spec samples do) until it reaches [3.6]-[4.5]$\sim$ 0.3 and [5.8]-[8.0]$\sim$ 1.3. At this point, the model grid abruptly turns to redder [3.6]-[4.5] colors, with [5.8]-[8.0] color not changing much. It is also seen that the C-rich AGB stars in the SAGE and SAGE-Spec samples are located in regions occupied by the densest concentrations of extreme AGB candidate points. One region is the "finger" of extreme AGB points extending from point ([3.6]-[4.5], [5.8]-[8.0]) = (0.3, 0.3) to (-0.2, 0.7), which is almost perpendicular to the finger of RSG candidate points. The other, more densely populated concentration of extreme AGB candidate points, in which are found many

C-rich AGBs from the SAGE-Spec sample, extends from (0.3, 0.3) to (1, 0.7). This suggests a large majority of sources in the SAGE sample identified as extreme AGBs have carbon-rich chemistry. As with the CMDs, there is an exception in the isolated O-rich AGB star IRAS 05298-6957 from the SAGE-Spec sample (and OH/IR sample; Marshall et al. 2004) at ([3.6]-[4.5],[5.8]-[8.0]) of (0.80, 0.91).

Amongst the O-rich AGB stars in the SAGE-Spec sample, the model grid provides mostly good coverage except for the bluest such sources. From the CMDs, we learn that the bluest sources are often the faintest, so we apply those lessons here. In the [8.0] versus [3.6]-[8.0] CMD, the faintest stars had [3.6]$\sim$ 12 and [8.0]$\sim$ 12.3. Assuming [3.6]-[4.5] = [5.8]-[8.0] = 0, then [4.5] = 12 and [5.8] = 12.3 typically for the blue O-rich AGB SAGE candidates not covered by the grid in this CCD. According to the SAGE Data Delivery document, the 1σ errors in [4.5] and [5.8] for these bluest stars are 0.04 and 0.07 magnitudes, respectively. This means the 3σ error in [3.6]-[4.5] could be up to $\sim$0.3 and that in [5.8]-[8.0] could be up to $\sim$0.4. Though strictly speaking only 3436 out of the 17769 O-rich AGB candidates from SAGE plotted here are covered by the model grid, all of the 17769 except the 6 with [3.6]-[4.5] $<$ -0.4, the $\sim$11 with [5.8]-[8.0] $<$ -0.35, and the $\sim$30 with [3.6]-[4.5] $>$ 0.4 separated from the densest concentration of O-rich AGB candidates from SAGE and bluer than the model grid are consistent with the model grid. The 17 bluest stars (6+11) not consistent with the model grid may be misidentified and may actually be C-rich AGB stars (see discussion in CMD subsections about the stars with the bluest colors). Similarly, the group of 30 may also be misidentified, as it has colors more like C-rich AGB stars from SAGE-Spec, C-rich AGB candidates from SAGE, and extreme AGB candidates (which we have already noted are more likely to have carbon-rich dust than oxygen-rich dust) from SAGE.

Only 38 out of 107 RSGs from SAGE, 21 out of 32 O-rich AGB candidates from SAGE-Spec, and 4 out of 18 RSGs from SAGE-Spec are covered by the grid. However, all the uncovered ones from these three populations are at most only 0.3 magnitudes separated from any edge of the grid coverage, so they are consistent with the model grid. Seven of the 10 OH/IR stars are covered by the grid. Two of the Marshall et al. (2004) OH/IR stars lie very close to the grid but just to slightly bluer [5.8]-[8.0] colors of it, IRAS 04545-7000 and IRAS 05003-6712. The edge of the grid is consistent with these two OH/IR stars, lying within their 3-σ errors. However, IRAS 05280-6910 is neither covered by the grid nor consistent with it, being located near (1.5, 2). The reason for this discrepancy is unknown, but we do note that the **2D**ust model of this star's SED by Boyer et al. (2010) indicates a very large total mass-loss rate from this star of a few times $10^{-3} M_{\odot} yr^{-1}$, consistent with this OH/IR star's very red colors in this CCD. Lastly, only 307 out of the 1423 extreme AGB candidates from SAGE plotted are covered by the model grid. However, as we noted previously, the extreme AGB stars may be more consistent with a carbon-rich dust chemistry

than oxygen-rich dust chemistry.

K_s-[8.0] versus K_s-[3.6]

In a very general sense, the K_s-[8.0] versus K_s-[3.6] CCD, plotted in Figure 6, is similar to the previous one, [5.8]-[8.0] versus [3.6]-[4.5]. At the bluest colors lie the O-rich AGB candidates. On top of them lie the RSG candidates from SAGE as well as both the O-rich AGB stars and RSGs from SAGE-Spec. These, as previously, form a locus of points around a line of highly positive slope. At redder colors lie the extreme AGB candidates. The O-rich AGB star from the SAGE-Spec sample (and OH/IR sample; Marshall et al. 2004), IRAS 05298-6957, lies at (3.87, 6.26), in the midst of the region dominated by extreme AGB candidate stars.

The bluest models provide good coverage of the RSG candidates from SAGE, the RSGs from SAGE-Spec, the densest concentration of O-rich AGB candidates from SAGE, and the O-rich AGB stars from SAGE-Spec. The coverage is better than for the [5.8]-[8.0] versus [3.6]-[4.5] CCD, though a number of O-rich AGB, extreme AGB, and RSG candidates from SAGE are not covered by the model grid. Using 1σ errors for the faintest stars cited in previous subsections for [3.6] and [8.0] and assuming a 1σ uncertainty of 0.02 magnitude for K_s=12 (Skrutskie et al. 2006), the 3-σ error for both K_s-[8.0] and K_s-[3.6] colors could be up to 0.3 magnitudes. Thus, all 17783 O-rich AGB candidates from SAGE plotted except $\sim$ 30 with K_s-[3.6] $<$ -0.2 and another $\sim$ 20 with K_s-[3.6] $\sim$ 1.1 and K_s-[8.0] $\sim$ 1.5 are consistent with the model grid. As concluded for the CMDs and for the previous CCD, the $\sim$ 30 with the bluest colors may be misidentified. The $\sim$ 20 with intermediate colors lie directly on top of a dense population of C-rich AGB candidates from SAGE (purple points), so they also may be misidentified as O-rich. Of the 108 RSG candidates from SAGE plotted, all but 1 are consistent with the grid. The 1 inconsistent one, with K_s-[3.6]$\sim$ -0.25, has a very blue color and may be misidentified. The 33 O-rich AGB stars and 18 RSG stars from SAGE-Spec plotted are all consistent with the model grid. In this CCD, 9 out of the 10 OH/IR stars from Marshall et al. (2004) are covered by the grid, and the discrepant one again is IRAS 05280-6910, which, as we noted earlier, has a very high mass-loss rate (Boyer et al. 2010).

As with the previous CCD, a majority of the extreme AGB candidates are not covered by the model grid. The model grid covers two O-rich AGB stars from SAGE-Spec at K_s-[3.6] colors of about 2 and 4, which are located in the middle of the extreme AGB region on the plot. These two O-rich AGB stars provide a test of the model grid at high optical depth, which it passes quite successfully. The model grid suggests a lower envelope to the K_s-[8.0] color of any extreme AGB stars with O-rich dust chemistry. This lower envelope can be described by the lines

$$\begin{aligned} K_s - [8.0] &= 5.13 \times (K_s - [3.6]) - 2.38 \qquad \text{for} \qquad K_s - [3.6] < 0.95 \ \text{ and} \\ K_s - [8.0] &= 1.28 \times (K_s - [3.6]) - 1.22 \qquad \text{for} \qquad K_s - [3.6] \geq 0.95 \ , \end{aligned} \tag{1}$$

such that the extreme AGB stars with lower K_s-[8.0] colors than these lines probably do not have O-rich dust chemistry, having C-rich dust chemistry instead. In total, 525 out of the 1283 extreme AGB candidates from SAGE plotted have K_s-[8.0] colors higher than this envelope. As C-rich AGB stars from SAGE-Spec are above the envelope in the extreme AGB region of the CCD, 525 is most likely an upper limit on the number of extreme AGB candidates in this plot that could have O-rich dust chemistry. Finally, we note the O-rich and C-rich AGB stars in the SAGE-Spec sample separate fairly well for K_s-[3.6] $\lesssim 1.3$; for redder K_s-[3.6] colors, AGB stars of the two chemistries in the SAGE-Spec sample mix together on the plot. Over most of the K_s-[3.6] colors spanned by the data plotted in Figure 6, the O-rich models have redder K_s-[8.0] colors than most of the extreme AGB candidates from SAGE, which overlap with a number of C-rich AGB stars from the SAGE-Spec sample. The O-rich stars having redder K_s-[8.0] colors is most likely due to the O-rich AGB stars having lower continuum emission over near-infrared wavelengths ($< 8\,\mu$m) relative to the flux from IRAC $8\,\mu$m (see discussion by Sargent et al. 2010) than is true for C-rich AGB stars (for which the dust emissivity monotonically decreases; Srinivasan et al., *in prep*). However, we note that, in general, this plot is less useful in separating the O-rich and C-rich evolved star populations in the SAGE-Spec sample than the [5.8]-[8.0] versus [3.6]-[4.5] CCD was.

[3.6]-[24] versus K_s-[3.6]

The final CCD we discuss, that of [3.6]-[24] versus K_s-[3.6] plotted in Figure 7, is somewhat different from the other two CCDs discussed here. The lower envelope to the [3.6]-[24] colors of the reddest models is described by the lines

$$\begin{aligned} [3.6] - [24] &= 7.5 \times (K_s - [3.6]) - 3.8 \qquad \text{for} \qquad K_s - [3.6] < 0.99 \ \text{ and} \\ [3.6] - [24] &= 0.55 \times (K_s - [3.6]) + 3 \qquad \text{for} \qquad K_s - [3.6] \geq 0.99 \ , \end{aligned} \tag{2}$$

where only 147 out of the 1223 extreme AGB candidates from SAGE plotted are above the lower envelope. Here, the O-rich AGB candidates stretch out in the direction of [3.6]-[24] while only narrowly spreading out over a very small range of K_s-[3.6]. As before, the 3-σ error on K_s-[3.6] is ~ 0.3. The 1-σ error on [24] for the faintest sources is up to ~ 0.5, while

that for [3.6] is $\sim$0.1 (see previous discussion), so the 3-σ error on [3.6]-[24] is up to $\sim$1.5. The 5566 O-rich AGB candidates from SAGE plotted are consistent with the model grid except for three groups. The $\sim$ 10 O-rich AGB SAGE candidates at the bluest K_s-[3.6] colors are likely misidentified, the $\sim$3 at the reddest [3.6]-[24] colors may suggest different T_{eff} or R_{min} than used in the model grid, and the $\sim$ 30 with K_s-[3.6] $\sim$ 1 and [3.6]-[24] $\sim$ 2.5 underneath the lower envelope may also be misidentified.

As for the [24] versus [8.0]-[24] CMD, we plot tracks for sets of models having all parameters at the same value except for τ_{10}, and we indicate the point for which $\tau_{10} = 1$. As with the [24] versus [8.0]-[24] CMD, the tracks show that τ_{10} has the greatest effect on the models, causing their colors to span almost the full range of both K_s-[3.6] and [3.6]-[24] colors covered by our model grid. As with the tracks on the CMD, the track bends at intermediate colors (K_s-[3.6] of $\sim$0.5) going from nearly vertical to a low positive slope. This bend is most likely due to the flattening of the model SED at mid-infrared wavelengths ($\sim 10\,\mu$m) due to the dust shell becoming optically thick at these wavelengths. For the track that begins furthest left (lowest K_s-[3.6] color) and ends with the lowest [3.6]-[24] colors, the parameters are set at $T_{eff} = 3700$ K, $R_{min} = 15\,R_{star}$, and luminosity of $16000 L_{\odot}$. The two tracks that begin at right (K_s-[3.6] > 0.5) both share $T_{eff} = 2100$ K, which shows, as the [24] versus [8.0]-[24] CMD showed, that T_{eff} has only a secondary effect on color, mildly altering the K_s-[3.6] color for the optically thinnest models (the points with the lowest [3.6]-[24] colors). Of the two tracks that begin at right, the one that reaches the greatest [3.6]-[24] colors for the optically thickest models (furthest to the right, or greatest K_s-[3.6] colors) has $R_{min} = 15\,R_{star}$ and luminosity of $4820 L_{\odot}$. The track that begins at right but ends at lower [3.6]-[24] colors for the optically thickest models has $R_{min} = 7\,R_{star}$ and luminosity of $57000 L_{\odot}$. These last two tracks demonstrate the effect of R_{min} on this CCD. The [3.6]-[24] color of the model with $\tau_{10} = 1$ and the greater R_{min} has a greater [3.6]-[24] color than the model with $\tau_{10} = 1$ and the lesser R_{min} because the model with greater R_{min} has cooler dust on average. Again, varying luminosity but no other parameters has no effect on CCDs because all wavelengths are multiplied by the same scalar to transform from a model with one luminosity to another.

We determined that the [3.6]-[24] colors of bare photospheres (stars without dust shells) were only $\sim$0.3 magnitudes lower than models having shells with $\tau_{10} = 8{\times}10^{-4}$. The accuracy and precision with which we will be able to determine the mass-loss rates for the AGB candidates in the SAGE sample with the smallest excesses over stellar photosphere emission will therefore be limited. However, we retain the models with τ_{10} between $1{\times}10^{-4}$ and $8{\times}10^{-4}$ because we will be better able to constrain mass-loss rates and other important parameters for stars with data having relatively small uncertainties. In subsequent studies we will use χ^2-minimization to determine the best fitting model to each SAGE candidate AGB star, and this procedure will determine the best-fit values and uncertainties of various

parameters of concern, including mass-loss rates. Including these low optical depth models can only add to the value of the χ^2-minimization analysis.

The RSG candidates form a nearly vertical column on top of the finger of O-rich AGB candidates extending from (0.3, 0) to (0.5, 3). Again, all 104 RSG candidates from SAGE plotted except the one with K_s-[3.6] of -0.25 are consistent with the model grid, while the one with negative color may be misidentified. The 17 RSGs and the 33 O-rich AGB stars from SAGE-Spec are consistent with the model grid. In this CCD, all 8 of the OH/IR stars from Marshall et al. (2004) with sufficient photometry to be plotted here are covered by the model grid.

Interestingly, many of the O-rich AGBs in the SAGE-Spec sample with K_s-[3.6] < 0.5 lie directly on top of the RSG candidate points. Even more promising, a dense concentration of model points lands on top of these O-rich AGB SAGE-Spec points and RSG candidate points. We interpret the stretching in the [3.6]-[24] direction of the O-rich AGB candidates, the RSG candidates, the bluest SAGE-Spec O-rich stars, and the bluest models in the grid as being due to the 3.6 μm band being optimally placed between the shorter wavelengths where the stellar emission dominates, and the longer wavelengths where dust emission dominates. Encouragingly, as with the other CCDs we discuss, the model points with the reddest K_s-[3.6] colors of 0.5 to 4 match the SAGE-Spec O-rich AGB star points quite well.

4.2. Verification of Model Grid by SED-Fitting

As further verification of the model grid presented here, we fit models from our O-rich evolved star grid to the photometry of various stars, anticipating future work fitting our model grid to the thousands of candidate O-rich AGB, RSG, and extreme AGB stars in the SAGE sample.

4.2.1. Optimal Model Fits to Selected Stars

First, we fit the two O-rich AGBs modeled previously, HV 5715 and SSTSAGE052206 (Sargent et al. 2010). This provides a check on the modeling of those two stars. To find the best fit of model to data from our model grid, we find the model from our final grid that has minimum χ^2 with respect to the observed broadband $IJHK_s$, IRAC, and MIPS 24 μm photometry. To allow for real stars' luminosities not being one of the 56 discrete values of luminosity in our final grid, we determine by another χ^2 minimization the scalar that we multiply by our best-fit model flux to obtain the best possible fit. This scalar is typically

only a few percent away from unity. This has the virtue of fitting models to photometric bands that have been used (except *I* and *H*) in CMDs and CCDs to verify the validity of the model grid presented here. Here, χ^2 is weighted by the photometric uncertainties.

For SSTISAGE1C J052206.92-715017.6 ("SSTSAGE052206"), the best fit obtained from our grid was with the model with luminosity L = $4900 L_{\odot}$ and $\tau_{10} = 0.10$. The dust mass-loss rate for this model is $2.1{\times}10^{-9} M_{\odot} yr^{-1}$. This model is plotted in Figure 8 with the MCPS *I*, 2MASS *JHK*$_{\rm s}$, and epoch 1 catalog IRAC and MIPS-24 photometry plotted for this object by Sargent et al. (2010). Overall, these parameter values are not very far away from those determined by Sargent et al. (2010) when modeling multi-epoch broadband photometry and the *Spitzer*-IRS SAGE-Spec spectrum. From that analysis, the best-fit model obtained had luminosity L = $5100 L_{\odot}$ and $\tau_{10} = 0.095$, with a dust mass-loss rate of $2.0{\times}10^{-9} M_{\odot} yr^{-1}$, so the dust mass-loss rate found here is only $\sim$5% above the value obtain by our best fit here. Sargent et al. (2010) were modeling additional data at *J*, *H*, and K_s bands that closely agreed with the 2MASS data over these bands, which effectively weighted the importance of these bands more strongly in achieving a good fit. Here, we only have the 2MASS data, so the near-infrared data overall constrains the best-fit model more weakly than that obtained by Sargent et al. (2010), resulting in a lower luminosity in the best-fit model here. In view of future studies, the most important parameters to determine are mass-loss rates and stellar luminosity. For SSTSAGE052206, both dust mass-loss rate and luminosity are determined by fitting models from the O-rich model grid to match within $\sim$10% of the values determined by Sargent et al. (2010).

For HV 5715 the best fit obtained from our grid was with the model with stellar photosphere luminosity L = $33000 L_{\odot}$ and $\tau_{10} = 0.026$. The dust mass-loss rate for this model is $1.5{\times}10^{-9} M_{\odot} yr^{-1}$. This fit is also shown in Figure 8. As with the previous figure, the model is plotted with the MCPS *I*, 2MASS *JHK*$_{\rm s}$, and epoch 1 catalog IRAC and MIPS-24 photometry plotted for this object by Sargent et al. (2010). The match between the best-fit model from our model grid and the photometry is of similar quality to that for SSTSAGE052206. The model presented for this object by Sargent et al. (2010) had luminosity L = $36\,000 L_{\odot}$ and $\tau_{10} = 0.012$. The dust mass-loss rate found for this star by Sargent et al. (2010) is $2.3{\times}10^{-9} M_{\odot} yr^{-1}$, so the dust mass-loss rate found here is $\sim$35% lower. This is most likely due to the restricted range of $R_{\rm min}$ that we chose for our model grid because it covers most of the range of dust shell inner radii expected for typical O-rich AGB stars (Höfner 2007). As noted by Sargent et al. (2010), this star is quite variable, and if only the lowest fluxes were fit, the luminosity of the best-fit model would be about $31000 L_{\odot}$, which is below what we get here. This is understandable, as the 2MASS fluxes over *J*, *H*, and $K_{\rm s}$ that we fit here are some of the lower fluxes fit by Sargent et al. (2010). The relative error bars over the IRAC bands are larger than those for *J*, *H*, and $K_{\rm s}$ or 24 μm, which may account for

the slight mismatching of model to data at 5.8 and 8.0 μm. The difference between the best fit to this object's data presented by Sargent et al. (2010) and that presented here may be understood by the additional photometry (and IRS spectrum) considered by Sargent et al. (2010), which more strongly weights the near-infrared and mid-infrared parts of the SED than is done here.

We also explore the ranges of parameters explored by our model grid by fitting the SEDs of individual stars. Figure 9 shows the best fits from our O-rich grid to the O-rich AGB star SSTISAGE1A J045947.31-694756.4 and the extreme AGB star SSTISAGE1A J053238.56-682522.2. The O-rich AGB star has an extremely low dust mass-loss rate of $7.2\times10^{-13}M_{\odot}yr^{-1}$, while the extreme AGB star has a very high dust mass-loss rate of $6.7\times10^{-7}M_{\odot}yr^{-1}$. This spans much of the range of dust mass-loss rates covered by our grid, as shown in Figure 1. Dust mass-loss rate is directly influenced by τ_{10}, so this justifies the large range of τ_{10} explored by our grid.

In Figure 10, we show best fits to two more stars - one with low luminosity and one with high luminosity. The low luminosity star, SSTISAGE1A J052039.50-700344.3, is an O-rich AGB star, while the high luminosity star, Parker 1684, is a RSG star. The best-fit model to the former has a luminosity of $2260L_{\odot}$, while the best-fit model to the latter has a luminosity of $131000L_{\odot}$. This justifies the large range of luminosities explored by the grid (Figure 1).

Figure 11 demonstrates the need for the range of stellar effective temperatures we explore in our grid. SSTISAGEMC J053320.85-673031.6, a RSG star, is best fit by a model with T_{eff} = 4100 K, while SSTISAGE1A J054041.69-661446.7, an O-rich AGB star, is best fit by a model with T_{eff} = 2500 K. In this Figure, one notes the obvious shift in the peak of the stellar emission from one star to the other. This helps justify the range of T_{eff} explored in this grid.

Finally, in Figure 12 we demonstrate with two O-rich AGB stars the need for the wide range of R_{min} we explore in our grid. SSTISAGE1A J052019.36-693529.0 is best fit by a model with R_{min} = 3 R_{star}, while SSTISAGE1A J052544.65-692740.4 is best fit by a model with R_{min} = 15 R_{star}. The relative contribution to the SED from warmer dust is greater than that for the latter. This explains why there is relatively more emission in excess of that from the stellar photosphere over the 4.5, 5.8 and 8.0 μm bands with respect to the excess at 24 μm for the former star than for the latter star. In fact, the observed photometry of the latter star suggests R_{min} perhaps somewhat larger than 15 R_{star}, as the [8.0]-[24] color of the data is redder than that in the best-fit model. However, we do not explore larger R_{min} due to theoretical considerations (Höfner 2007).

4.2.2. Comparison to Other Modeling Efforts

In addition to justifying the range of parameters we explore in our model grid, we also test two of the most important parameters obtained from fitting SEDs with our models, luminosity and dust mass-loss rate. We test the values we obtain for these against the values obtained for the same stars by van Loon et al. (1999) and Groenewegen et al. (2009) (only some of the stars in the two M-star target sets are common to both). The coordinates for the M stars with and without *ISO* spectra from van Loon et al. (1999) were matched against the SAGE epoch 1 catalog. In all cases except two, the 3.6, 8.0, and 24 μm fluxes of the closest SAGE source to the van Loon et al. (1999) position matched fairly well the 3.6, 8.0, and 24 μm model fluxes plotted by van Loon et al. (1999). The two for which the closest SAGE match did not match in these infrared fluxes were IRAS 05329-6708 and SP77 30-6. The former was much better matched to a SAGE source $\sim 27''$ away than the one $<1''$ away. The mid-infrared data fitted by van Loon et al. (1999) for this source are a spectrum and photometry from the *Infrared Space Observatory* (ISO; Kessler et al. 1996). ISO had lower resolution than *Spitzer*, which may allow this large discrepancy in position. The nearest SAGE match to the position of the latter target, SP77 30-6, was $\sim 8''$ away, but the nearest SAGE source of comparable mid-infrared fluxes to those plotted by van Loon et al. (1999) for this star was $\sim 14''$ away. We used the latter SAGE match as the data for this star. Groenewegen et al. (2009) fit models to data that includes SAGE *Spitzer* data, so the matching between each Groenewegen et al. (2009) position and the closest SAGE position is very likely the correct one. We remove IRAS 04509-6922 from our analysis, as the only flux available for its match in the SAGE catalog that we consider is the 24 μm flux, which is not enough to constrain its model.

In Figure 13 we compare luminosities obtained by the modeling done by van Loon et al. (1999) and Groenewegen et al. (2009) to those from the best fits of our model O-rich grid to each of the ones from van Loon et al. (1999) and Groenewegen et al. (2009) considered. As may be noted in the plot, the luminosities obtained by **2D**ust modeling are within a factor of ~ 2 of those obtained by van Loon et al. (1999) or Groenewegen et al. (2009). This is a fairly good correspondence, considering the factors that may contribute to obtaining different luminosities from our modeing versus the modeling by the other two studies. These factors include variability, the use of different types of data (we only use one epoch of photometry at each band in each SED, while the other authors also use spectroscopy; Groenewegen et al. 2009, additionally use photometry from multiple epochs), etc.

In Figure 14 we compare the dust mass-loss rates obtained by the two other modeling studies to those from our model grid. The output of **2D**ust is dust mass-loss rate, so we convert the total mass-loss rates reported by van Loon et al. (1999) and from Groenewegen

et al. (2009) to dust mass-loss rates by dividing their total mass-loss rates by their assumed gas-to-dust ratios of 500 and 200, respectively. Here we see a difference between the target sets obtained from van Loon et al. (1999) and from Groenewegen et al. (2009). The matching between dust mass-loss rates obtained from our **2D**ust grid and those stars fit by van Loon et al. (1999) is reasonable (a factor of ~ 3) over many orders of magnitude of dust mass-loss rate. As noted previously, the best SAGE match to the fluxes plotted by van Loon et al. (1999) for IRAS 05329-6708 come not from the closest SAGE match but instead from $\sim 27''$ away (again, not implausible due to the lower ISO resolution). Overall, our modeling agrees fairly well with that done by van Loon et al. (1999).

Figure 14 shows the dust mass-loss rates obtained by **2D**ust to be comparable to those obtained by Groenewegen et al. (2009) at the highest dust mass-loss rates of $\sim 10^{-7} M_{\odot} yr^{-1}$. However, at lower dust mass-loss rates the values obtained by **2D**ust begin to exceed those obtained by Groenewegen et al. (2009), building up to a factor of ~ 6 deviation for Groenewegen et al. (2009) dust mass-loss rates near $\sim 2 \times 10^{-9} M_{\odot} yr^{-1}$. It is difficult to identify the reason for this discrepancy. We found that the optical depths at $10\,\mu$m we obtain when modeling the Groenewegen et al. (2009) targets are also greater than those obtained by Groenewegen et al. (2009) for the ones with lower optical depths. For the ones with higher optical depths, the optical depths we obtain are similar to those Groenewegen et al. (2009) obtained. The pattern of disagreement between our modeling and that of Groenewegen et al. (2009) is similar for both optical depth and dust mass-loss rate. Both our modeling and that of van Loon et al. (1999) do not fit data shortward of *I*-band, while the Groenewegen et al. (2009) modeling does. As an experiment, we tried fitting the *UBV* data in addition to the infrared data we already include in our fitting. This resulted in slightly lower dust mass-loss rates, but not enough to explain the factor of 6 discrepancy. Another difference is that van Loon et al. (1999) and we only use a single type of dust in our modeling, while Groenewegen et al. (2009) use multiple sources for their dust optical properties. However, there was no apparent pattern showing different types of dust used by Groenewegen et al. (2009) to correspond to any range of dust mass-loss rate. Groenewegen et al. (2009) used *Spitzer*-IRS spectra to constrain their modeling, while neither van Loon et al. (1999) nor we did (though van Loon et al. 1999, used ISO spectra). The $8\,\mu$m flux we use only partially covers the $10\,\mu$m silicate band, so our only fitting photometry likely leaves our modeling less accurate when fitting low mass-loss rate stars' SEDs. However, we note the few van Loon et al. (1999) sources with low dust mass-loss rates agree fairly well with the dust mass-loss rates from our **2D**ust modeling. When *Akari* (Murakami et al. 2007) data is made public, the addition of that data to the SAGE data will significantly help constrain our modeling of O-rich evolved stars. We do note that Srinivasan et al. (2009) found the highest mass-loss rate AGB stars contribute the most to the dust mass return to the LMC, so it is encouraging

that our modeling agrees with that of both van Loon et al. (1999) and Groenewegen et al. (2009) for the highest dust mass-loss rate stars. Finally, in Figure 15 we show the SED fits from our modeling to stars that were fit by both van Loon et al. (1999) and Groenewegen et al. (2009). These two stars are HV 888 and IRAS 05402-6956. Our models of each of these fit the data quite well, which lends more support to the validity of our modeling.

5. Conclusions

With the goal of quantifying the mass-loss of O-rich evolved stars in the LMC in mind, we have constructed a grid of models of these stars. To begin, we construct a grid of 1225 models using **2D**ust. This grid assumes for each model a spherically symmetric shell of dust surrounding a star whose spectrum is assumed to be that of a PHOENIX model (Kučinskas et al. 2005, 2006) with stellar effective temperature between 2100 K and 4700 K and log(g) = -0.5. This initial grid of $\sim$1200 models has already excluded models whose dust temperature at the dust shell inner radius was above 1400 K on the basis of being unphysical, as this is approximately the sublimation temperature of silicate dust. Four values of R_{min} are explored in the grid – 3, 7, 11, and 15 R_{star}. We explore values of optical depth at 10.0 μm wavelength, τ_{10}, between 10^{-4} and 26. The mass loss is assumed to be constant over time, and the dust properties assumed are those used for the models of HV 5715 and SSTSAGE052206 reported by Sargent et al. (2010). This initial grid was computed by running the **2D**ust models on the Royal computer cluster at STScI. We scale our models, as described in §2.2, to create the final grid of 68600 models from the initial grid. For each combination of T_{eff}, R_{min}, and τ_{10} in the initial grid, the full grid has 56 values of luminosity ranging from 10^3–$10^6 L_\odot$ with finer gridding in luminosity for luminosities between 10^3–$2\times10^4 L_\odot$.

From this final grid, colors and magnitudes are synthesized from the model spectra and compared to the observed colors and magnitudes of O-rich AGB, RSG, and extreme AGB candidates in the SAGE sample and of a small sample of OH/IR stars from Marshall et al. (2004). The coverage of the observed data by the models is generally very good. Almost all of the observed data is consistent with the model grid. The very few data points that are not consistent often are likely misidentifications, while a few of these may suggest stars with dust shells with parameters somewhat outside the range explored in our grid. The extreme AGB candidate points are covered well in the CMDs but poorly in the CCDs, suggesting the composition of their dust typically disagrees with that assumed for our model grid (i.e., silicates). The SAGE-Spec data, when overlaid on the CMDs and CCDs, lend further support to these ideas – our model grid typically covers the SAGE-Spec O-rich AGBs quite well over wide color and magnitude ranges, and most of the extreme AGB candidates are more

consistent with C-rich AGBs in the SAGE-Spec sample than O-rich AGBs in the SAGE-Spec sample. Further, our optically thicker models are largely consistent with a small sample of OH/IR stars from the study by Marshall et al. (2004). We determine lower envelopes to the K_s-[8.0] and [3.6]-[24] colors as a function of K_s-[3.6] color for which extreme AGB star colors could be consistent with the colors of the models in our oxygen-rich model grid. We also wish to note that the close general matching of our model grid to the observed data in CMDs and CCDs gives further support for the dust properties assumed in modeling O-rich evolved stars by Sargent et al. (2010).

Finally, our model grid has been tested by finding the best fit model from the grid to each of the photometric SEDs of stars modeled by van Loon et al. (1999), Groenewegen et al. (2009), and Sargent et al. (2010). The quality of fit of model fluxes to observed fluxes is quite good. The matching between luminosity, τ_{10}, and dust mass-loss rate found for HV 5715 and especially SSTSAGE052206 by our best-fit model here and by the models obtained by Sargent et al. (2010) is fairly close. Also, our modeling is found to be consistent with that of M stars by van Loon et al. (1999) and fairly consistent with that of M stars by Groenewegen et al. (2009). This provides verification of the model grid presented in this paper.

This work is based on observations made with the *Spitzer Space Telescope*, which is operated by the Jet Propulsion Laboratory, California Institute of Technology under NASA contract 1407. We acknowledge funding from the NAG5-12595 grant, SAGE-LMC *Spitzer* grant 1275598, SAGE-SEEDS *Spitzer* grant 1310534, and Herschel/HERITAGE grant 1381522. This publication makes use of the Jena-St. Petersburg Database of Optical Constants (Henning et al. 1999). The authors would also like to thank Kevin Volk for helpful comments and discussion. We wish to thank Peter Hauschildt for his assistance with the PHOENIX stellar photosphere models. The authors have made use of the SIMBAD astronomical database and would like to thank those responsible for its upkeep. The authors also would like to thank Bernie Shiao at STScI for his hard work on the SAGE database and his kind assistance.

REFERENCES

Bernard, J.-P., et al. 2008, AJ, 136, 919

Blum, R. D., et al. 2006, AJ, 132, 2034

Bonanos, A. Z., et al. 2009, AJ, 138, 1003

Bowen, G. H. 1988, ApJ, 329, 299

Boyer, M. L., et al. 2010, A&A, 518, L142

Busso, M., Guandalini, R., Persi, P., Corcione, L., & Ferrari-Toniolo, M. 2007, AJ, 133, 2310

Cioni, M.-R. L., van der Marel, R. P., Loup, C., & Habing, H. J. 2000, A&A, 359, 601

Cohen, M., Wheaton, W. A., & Megeath, S. T. 2003, AJ, 126, 1090

Dufour, R. J., Shields, G. A., & Talbot, R. J., Jr. 1982, ApJ, 252, 461

Fazio, G. G., et al. 2004, ApJS, 154, 10

Feast, M. 1999, PASP, 111, 775

Ferrarotti, A. S., & Gail, H.-P. 2006, A&A, 447, 553

Feuchtinger, M. U., Dorfi, E. A., & Hofner, S. 1993, A&A, 273, 513

Fleischer, A. J., Gauger, A., & Sedlmayr, E. 1991, A&A, 242, L1

Fleischer, A. J., Gauger, A., & Sedlmayr, E. 1992, A&A, 266, 321

Gail, H.-P., Zhukovska, S. V., Hoppe, P., & Trieloff, M. 2009, ApJ, 698, 1136

González-Lópezlira, R. A., Bruzual-A., G., Charlot, S., Ballesteros-Paredes, J., & Loinard, L. 2010, MNRAS, 403, 1213

Groenewegen, M. A. T. 2006, A&A, 448, 181

Groenewegen, M. A. T., Sloan, G. C., Soszyński, I., & Petersen, E. A. 2009, A&A, 506, 1277

Gruendl, R. A., & Chu, Y.-H. 2009, ApJS, 184, 172

Harrington, J. P., Monk, D. J., & Clegg, R. E. S. 1988, MNRAS, 231, 577

Henning, T., Il'In, V. B., Krivova, N. A., Michel, B., & Voshchinnikov, N. V. 1999, A&AS, 136, 405

Hoefner, S., & Dorfi, E. A. 1997, A&A, 319, 648

Hoefner, S., Jorgensen, U. G., Loidl, R., & Aringer, B. 1998, A&A, 340, 497

Höfner, S. 2007, Why Galaxies Care About AGB Stars: Their Importance as Actors and Probes, 378, 145

Höfner, S. 2009, American Institute of Physics Conference Series, 1094, 872

Houck, J. R., et al. 2004, ApJS, 154, 18

Ivezic, Z., & Elitzur, M. 1995, ApJ, 445, 415

Jeong, K. S., Winters, J. M., Le Bertre, T., & Sedlmayr, E. 2003, A&A, 407, 191

Kessler, M. F., et al. 1996, A&A, 315, L27

Kim, S.-H., Martin, P. G., & Hendry, P. D. 1994, ApJ, 422, 164

Kučinskas, A., Hauschildt, P. H., Ludwig, H.-G., Brott, I., Vansevičius, V., Lindegren, L., Tanabé, T., & Allard, F. 2005, A&A, 442, 281

Kučinskas, A., Hauschildt, P. H., Brott, I., Vansevičius, V., Lindegren, L., Tanabé, T., & Allard, F. 2006, A&A, 452, 1021

Marigo, P., Girardi, L., Bressan, A., Groenewegen, M. A. T., Silva, L., & Granato, G. L. 2008, A&A, 482, 883

Marshall, J. R., van Loon, J. T., Matsuura, M., Wood, P. R., Zijlstra, A. A., & Whitelock, P. A. 2004, MNRAS, 355, 1348

Massey, P. 2003, ARA&A, 41, 15

Matsuura, M., et al. 2009, MNRAS, 396, 918

McDonald, I., van Loon, J. T., Decin, L., Boyer, M. L., Dupree, A. K., Evans, A., Gehrz, R. D., & Woodward, C. E. 2009, MNRAS, 394, 831

Meixner, M., et al. 2006, AJ, 132, 2268

Murakami, H., et al. 2007, PASJ, 59, 369

Nikolaev, S., & Weinberg, M. D. 2000, ApJ, 542, 804

Ossenkopf, V., Henning, T., & Mathis, J. S. 1992, A&A, 261, 567

Posch, T., Mutschke, H., Trieloff, M., & Henning, T. 2007, ApJ, 656, 615

Rieke, G. H., et al. 2004, ApJS, 154, 25

Sandage, A., & Walker, M. F. 1966, ApJ, 143, 313

Sargent, B. A., et al. 2010, ApJ, 716, 878, "Paper II"

Schlegel, D. J., Finkbeiner, D. P., & Davis, M. 1998, ApJ, 500, 525

Skrutskie, M. F., et al. 2006, AJ, 131, 1163

Srinivasan, S., et al. 2009, AJ, 137, 4810, "Paper I"

Srinivasan, S., et al. 2010, arXiv:1009.2681, "Paper III"

Ueta, T., & Meixner, M. 2003, ApJ, 586, 1338

van Loon, J. Th., Groenewegen, M. A. T., de Koter, A., Trams, N. R., Waters, L. B. F. M., Zijlstra, A. A., Whitelock, P. A., & Loup, C. 1999, A&A, 351, 559

Verhoelst, T., van der Zypen, N., Hony, S., Decin, L., Cami, J., & Eriksson, K. 2009, A&A, 498, 127

Volk, K., & Kwok, S. 1988, ApJ, 331, 435

Weinberg, M. D., & Nikolaev, S. 2001, ApJ, 548, 712

Werner, M. W., et al. 2004, ApJS, 154, 1

Whitney, B. A., et al. 2008, AJ, 136, 18

Winters, J. M., Fleischer, A. J., Le Bertre, T., & Sedlmayr, E. 1997, A&A, 326, 305

Winters, J. M., Le Bertre, T., Jeong, K. S., Helling, C., & Sedlmayr, E. 2000, A&A, 361, 641

Woods, P. M., et al. 2010, MNRAS, 1801

This preprint was prepared with the AAS LaTeX macros v5.2.

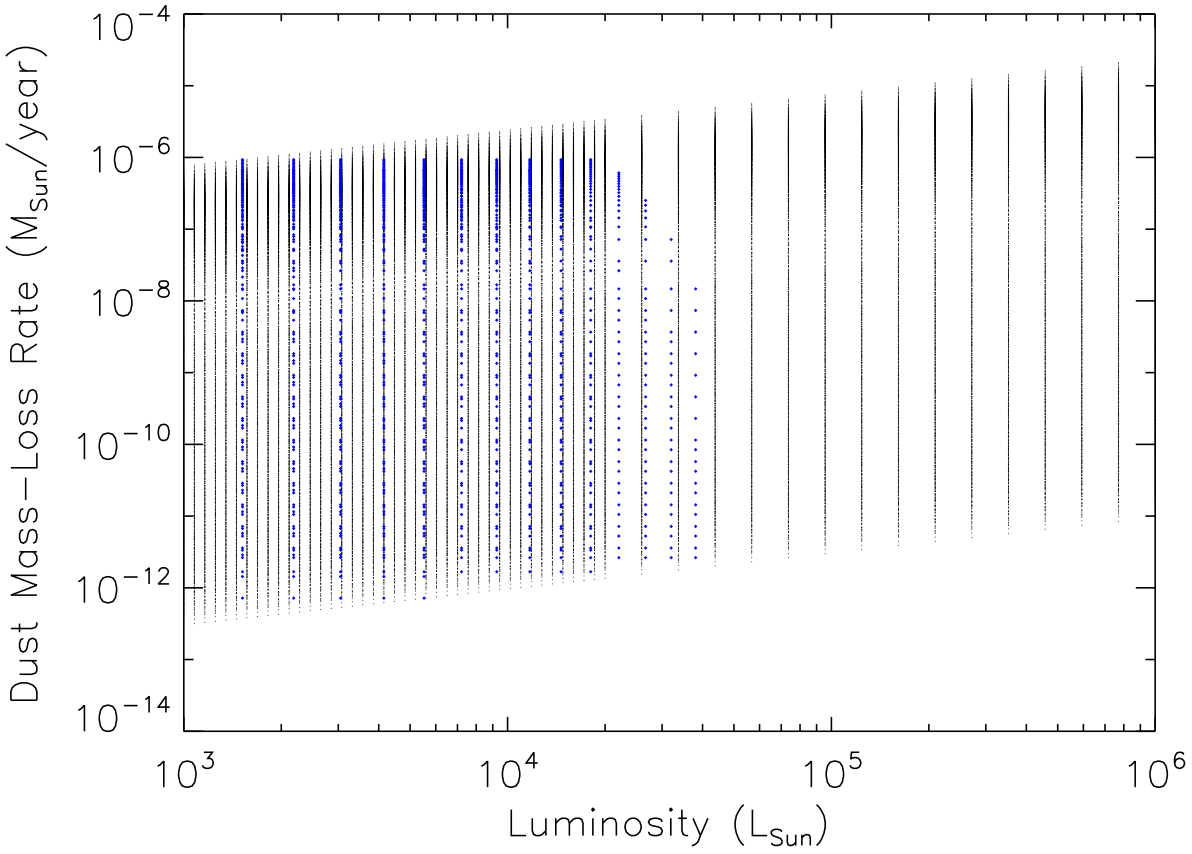

Fig. 1.— $\dot{M}_{dust}$ versus stellar luminosity for the models in our initial and final grids. The points corresponding to the initial grid are blue, and the points corresponding to the final grid are black. The $\dot{M}_{dust}$ is in $M_{\odot}yr^{-1}$, and the luminosities are in $L_{\odot}$.

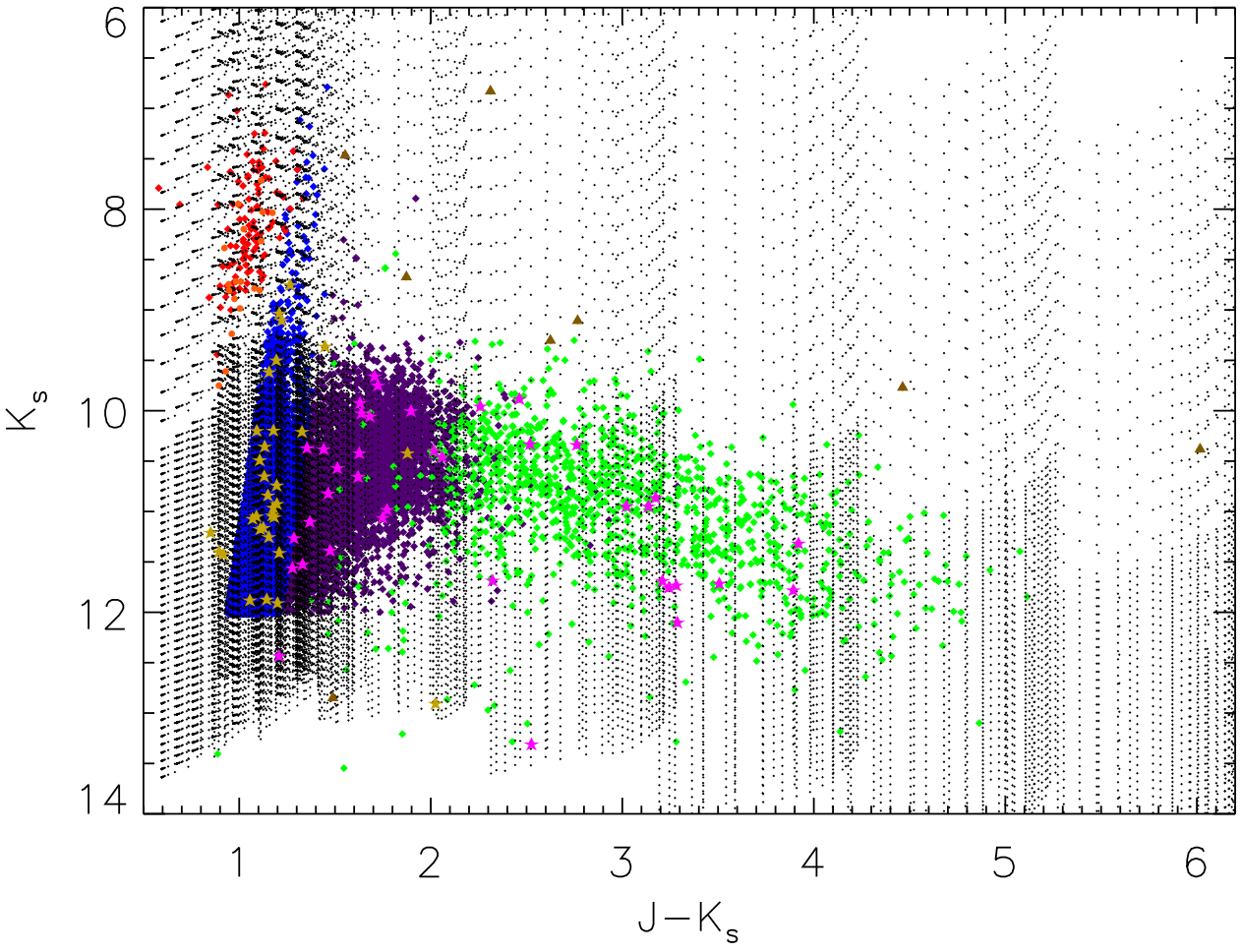

Fig. 2.— K_s versus J-K_s color-magnitude diagram. Of the observed sources in the SAGE sample, blue diamonds are oxygen-rich AGB candidates, red diamonds are RSG candidates, purple diamonds are C-rich AGB candidates, and green diamonds are extreme AGB candidates. The small black points are **2D**ust models from our final model grid (points for the initial grid are not shown in this figure or in any of the following figures). Of the SAGE-Spec sources, the O-rich AGB stars are gold star symbols, the RSGs are orange circles, and the C-rich AGB stars are magenta star symbols. OH/IR stars from Marshall et al. (2004) are brown triangles.

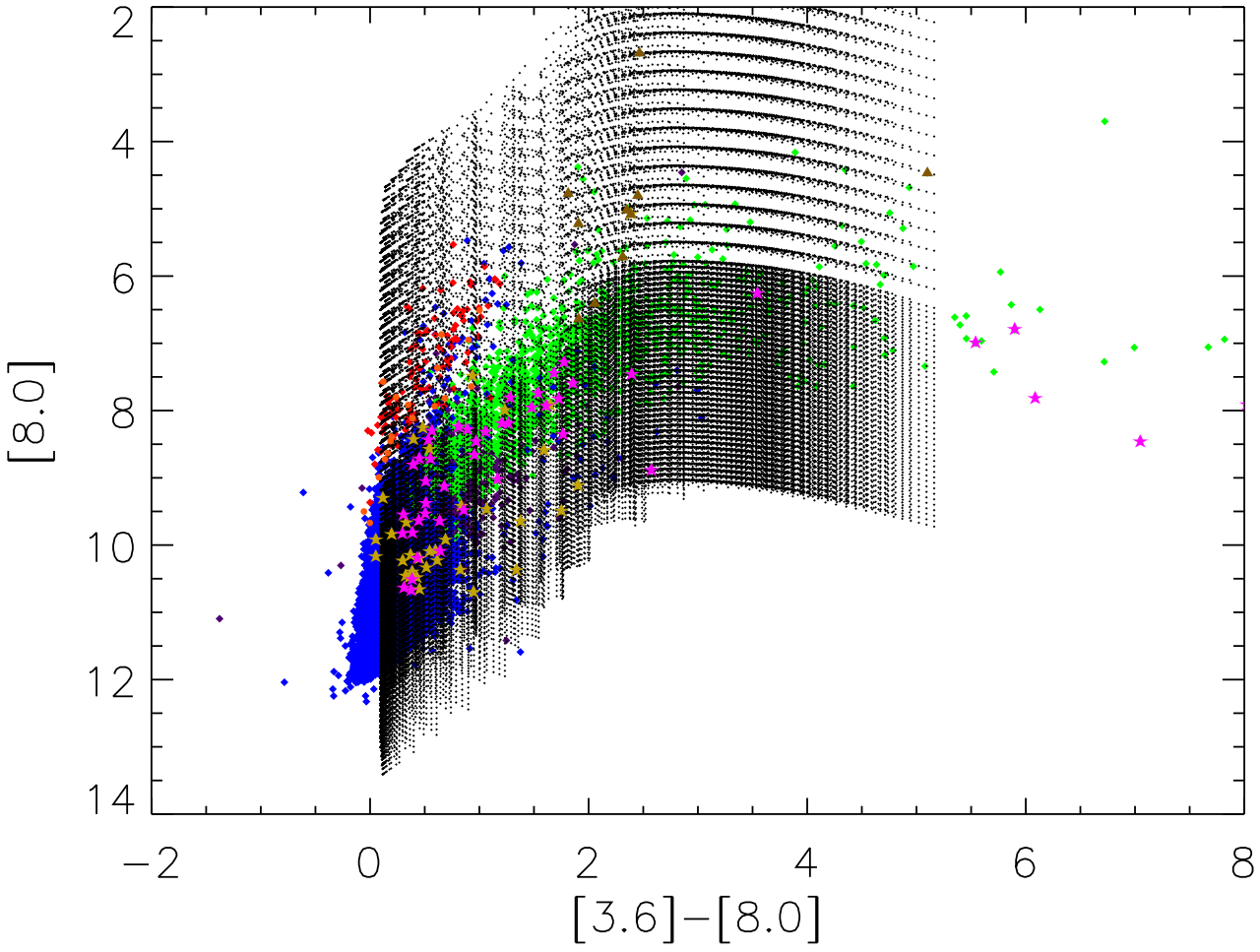

Fig. 3.— [8.0] versus [3.6]-[8.0] color-magnitude diagram. Same symbol convention as Figure 2.

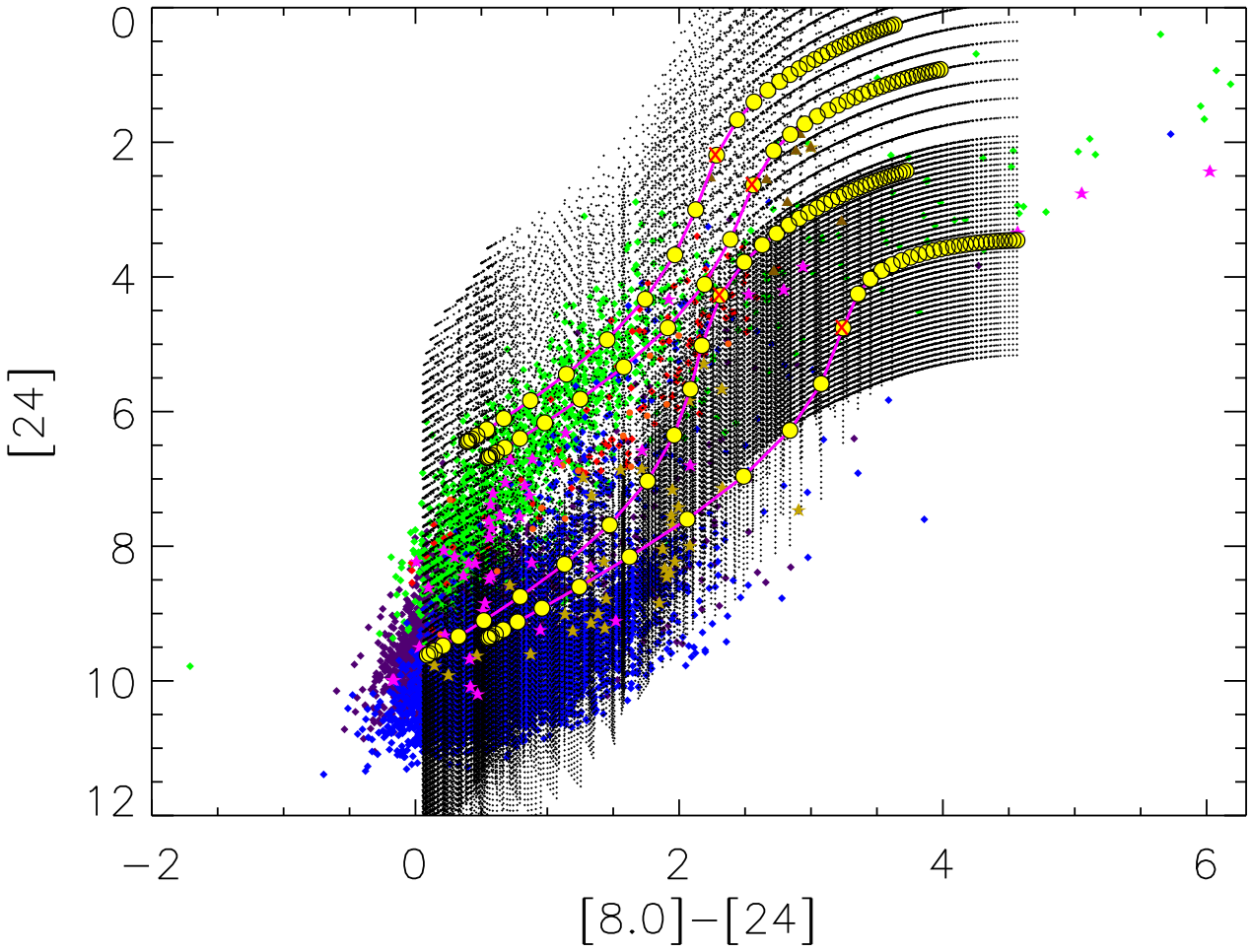

Fig. 4.— [24] versus [8.0]-[24] color-magnitude diagram. Same symbol convention as Figure 2. The magenta lines with yellow points overplotted are each a track for a set of models with the same T_{eff}, R_{min}, and luminosity, with the point corresponding to the model with $\tau_{10} = 1$ indicated with a red "x" on top of it. The lowest track (greatest [24] or lowest fluxes) has $T_{eff} = 2100\,K$, $R_{min} = 15\,R_{star}$, and $L = 4800 L_{\odot}$. The next highest track has $T_{eff} = 3700\,K$, $R_{min} = 15\,R_{star}$, and $L = 16000 L_{\odot}$. The second highest track has $T_{eff} = 2100\,K$, $R_{min} = 7\,R_{star}$, and $L = 57000 L_{\odot}$. The highest track has $T_{eff} = 2700\,K$, $R_{min} = 7\,R_{star}$, and $L = 120000 L_{\odot}$.

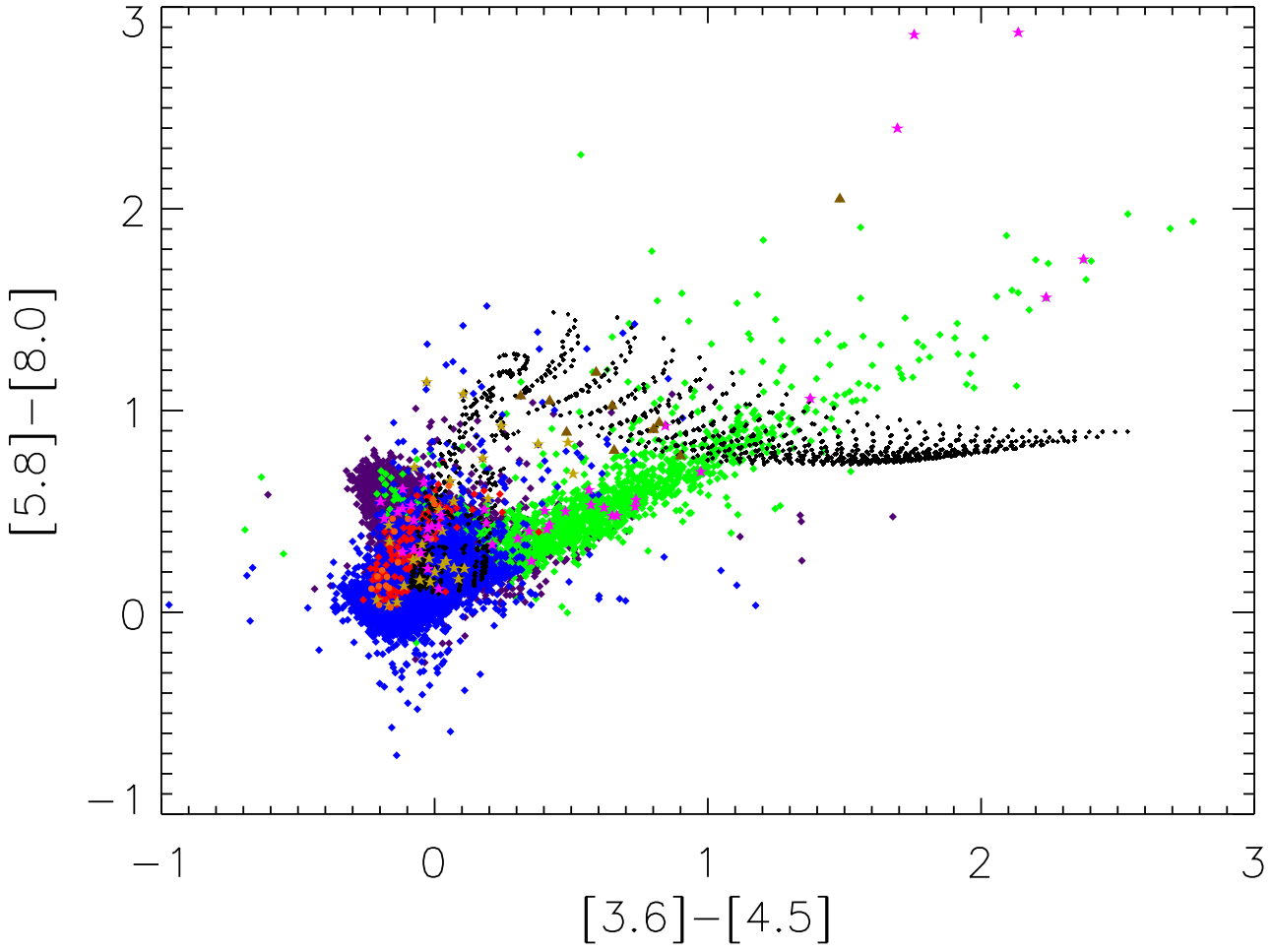

Fig. 5.— [5.8]-[8.0] versus [3.6]-[4.5] color-color diagram. Same symbol convention as Figure 2.

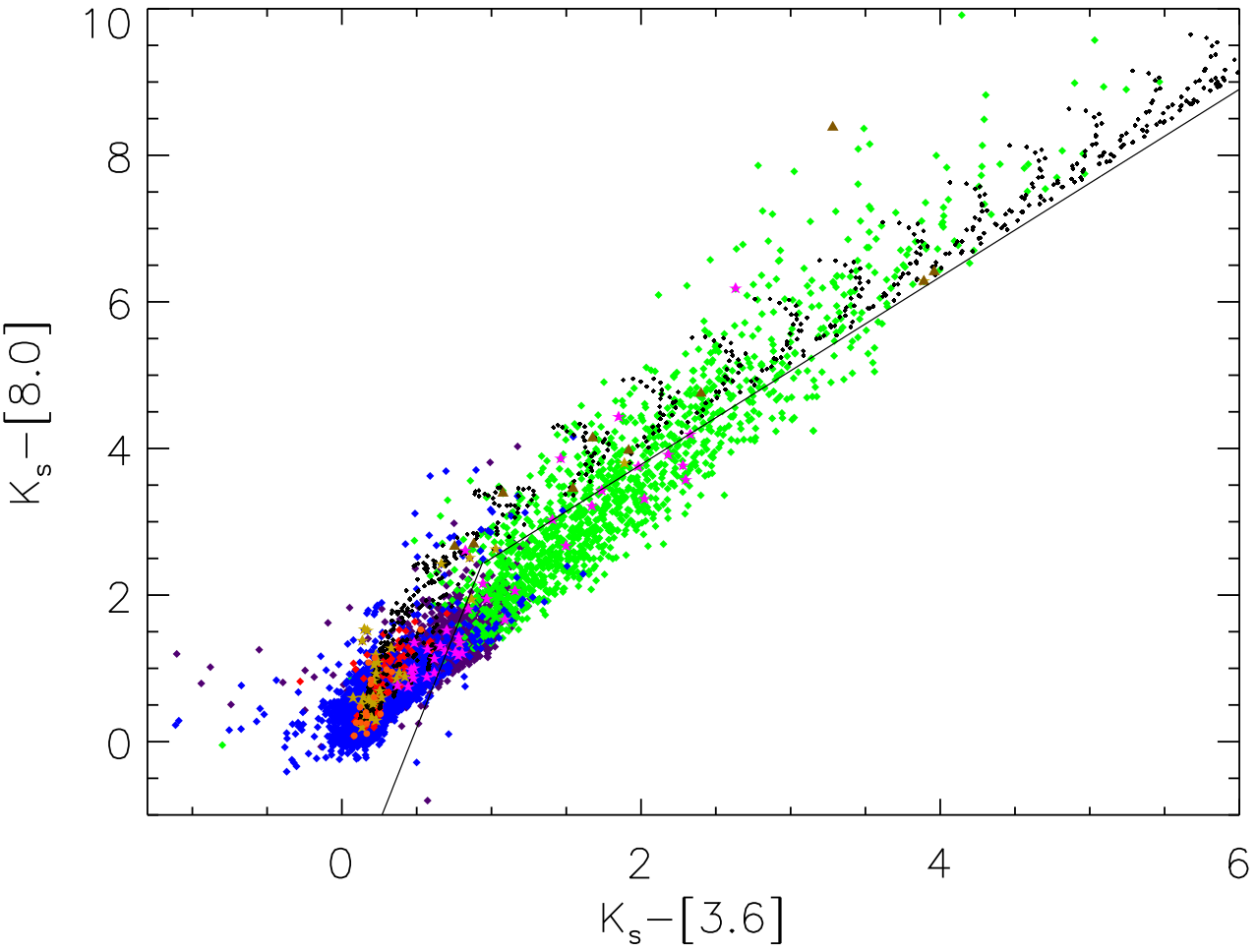

Fig. 6.— K_s-[8.0] versus K_s-[3.6] color-color diagram. Same symbol convention as Figure 2. The black lines indicate the K_s-[8.0] colors bluer than which there are no models in our oxygen-rich grid.

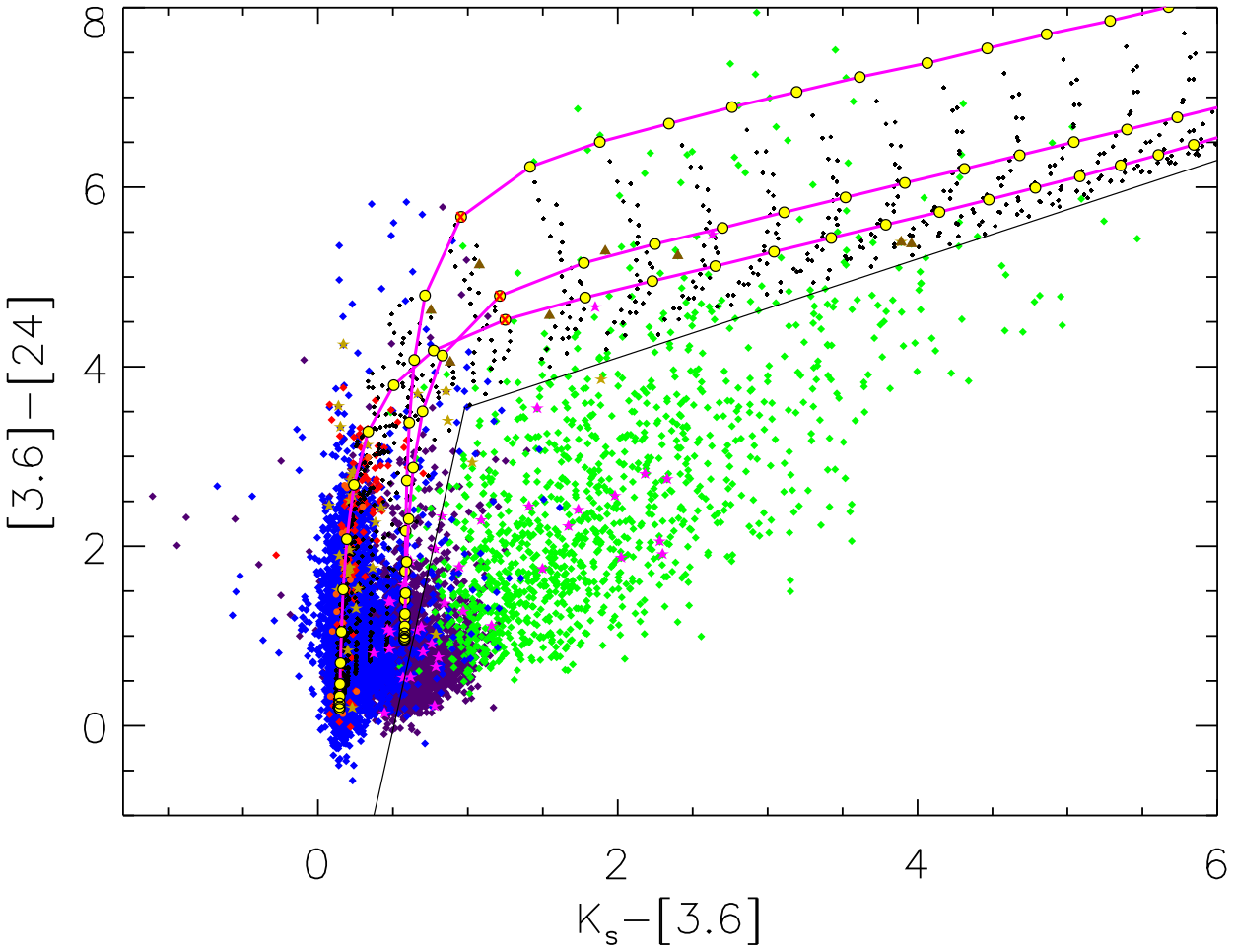

Fig. 7.— [3.6]-[24] versus K_s-[3.6] color-color diagram. Same symbol convention as Figure 2. The black lines indicate the [3.6]-[24] colors bluer than which there are no models in our oxygen-rich grid. The magenta line with yellow points overplotted is a track for a set of models with the same T_{eff}, R_{min}, and luminosity, with the point corresponding to the model with $\tau_{10} = 1$ indicated with a red "x" on top of it. The track beginning at left (lowest K_s-[3.6] color) has $T_{eff} = 3700\,K$, $R_{min} = 15\,R_{star}$, and $L = 16000 L_{\odot}$. The track that begins at slightly higher (redder) K_s-[3.6] color and ends at the greatest [3.6]-[24] colors has $T_{eff} = 2100\,K$, $R_{min} = 15\,R_{star}$, and $L = 4800 L_{\odot}$. The other track has $T_{eff} = 2100\,K$, $R_{min} = 7\,R_{star}$, and $L = 57000 L_{\odot}$.

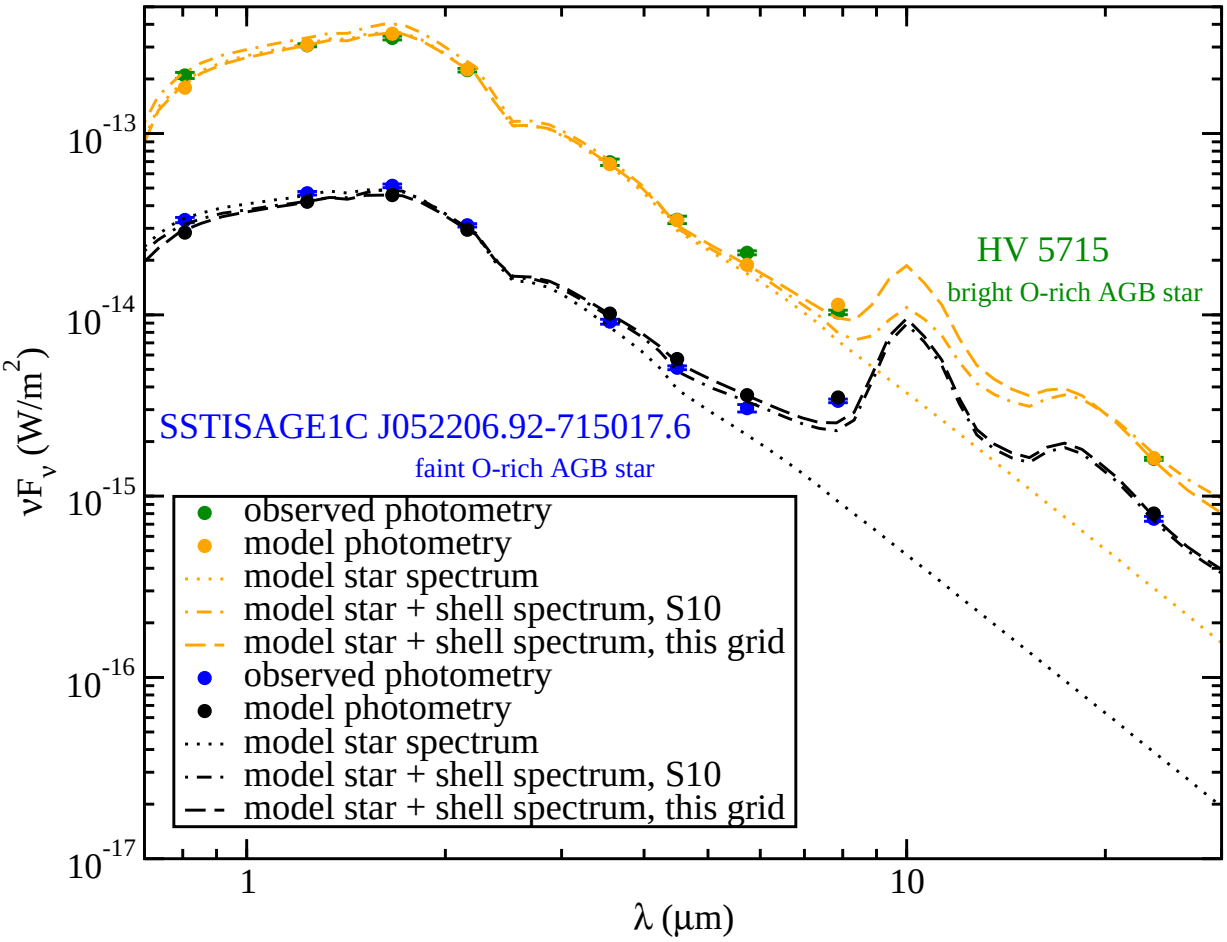

Fig. 8.— Best-fit models from O-rich evolved star grid fit to broadband photometry of each of bright and faint O-rich AGB stars (HV 5715 and SSTISAGE1C J052206.92-715017.6, respectively) fit by Sargent et al. (2010). Green points are observed photometry for bright O-rich AGB star, while orange points and the orange dashed line are the best fit model for this star. Similarly, blue points are observed photometry for faint O-rich AGB star, and black points and the black dashed line are the best fit model for this star. For each of the models, large points are the broadband photometry synthesized from the best-fit model, the dashed line is the spectrum of that model, and the dotted line is the spectrum of the stellar photosphere for that model. The two dash-dot lines are the best fits to the bright and faint O-rich AGB stars from Sargent et al. (2010), and they are indicated in the legend by "S10".

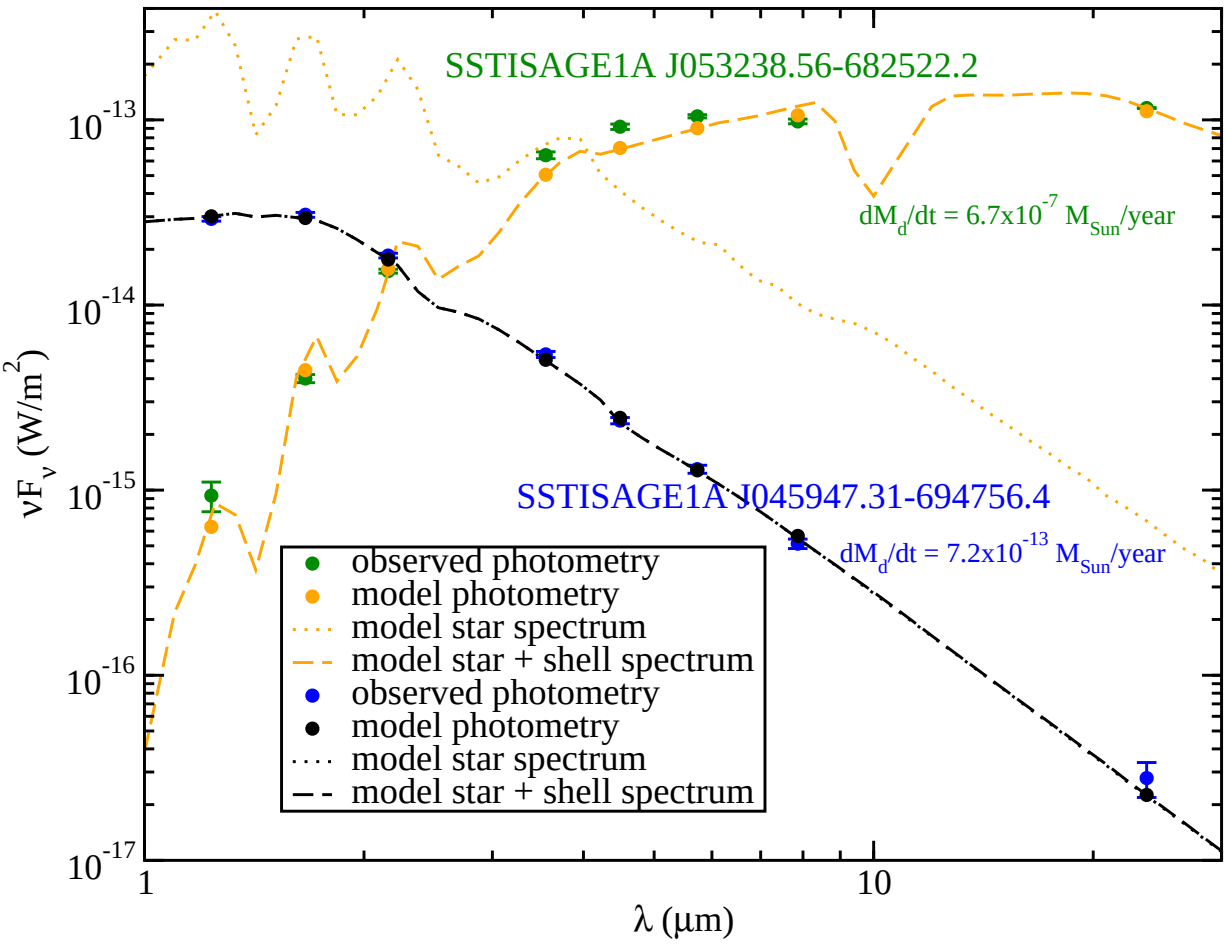

Fig. 9.— Best fit models from O-rich evolved star grid fit to broadband photometry of stars with very high and very low mass-loss rates. Green points are observed photometry for star with very high mass-loss rate, while orange lines are the best fit model for this star. Similarly, blue points are observed photometry for star with very low mass-loss rate, and black lines are the best fit model for this star. The same symbol convention as was used for Figure 8 is used here.

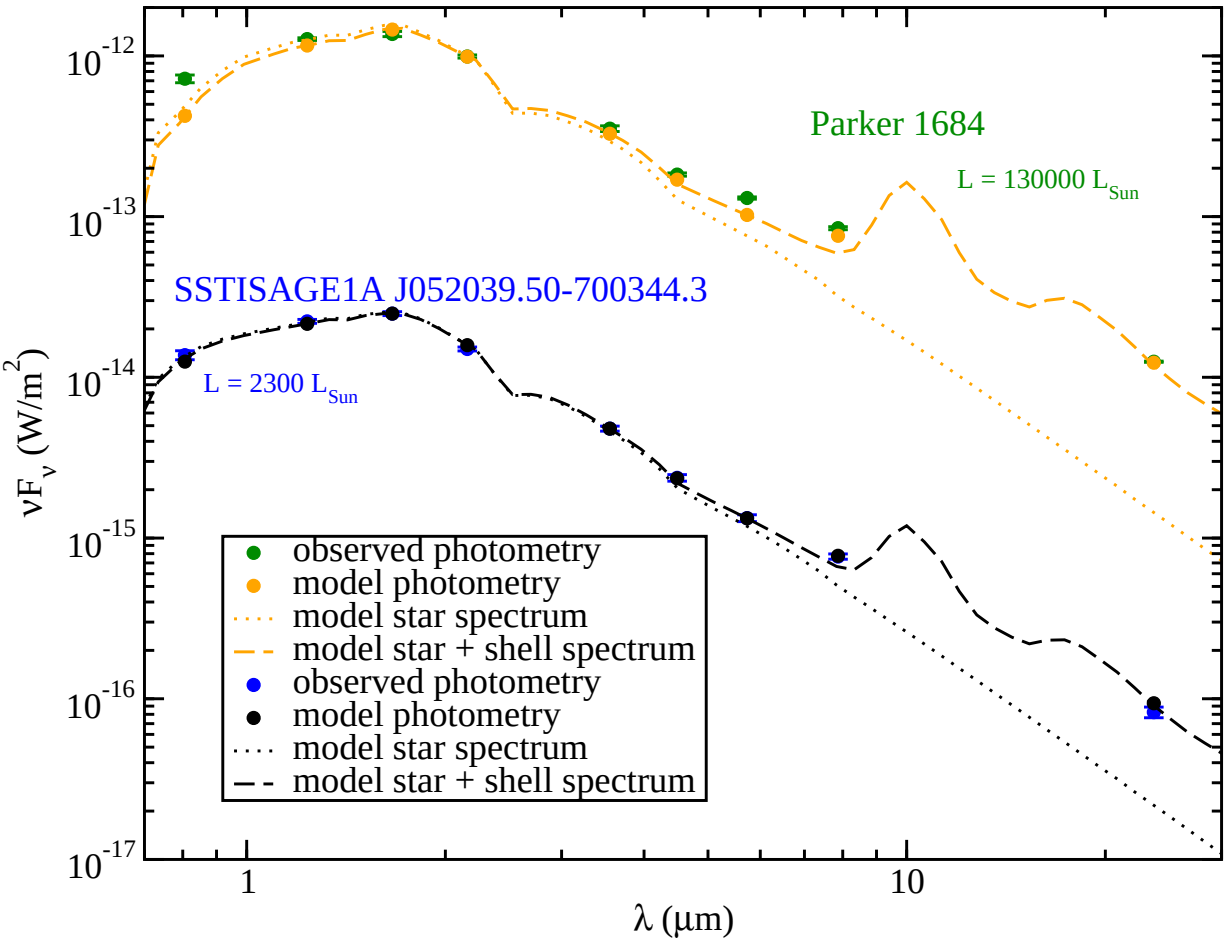

Fig. 10.— Best fit models from O-rich evolved star grid fit to broadband photometry of stars with very high and very low luminosities. Green points are observed photometry for star with very high luminosity, while orange lines are the best fit model for this star. Similarly, blue points are observed photometry for star with very low luminosity, and black lines are the best fit model for this star. The same symbol convention as was used for Figure 8 is used here.

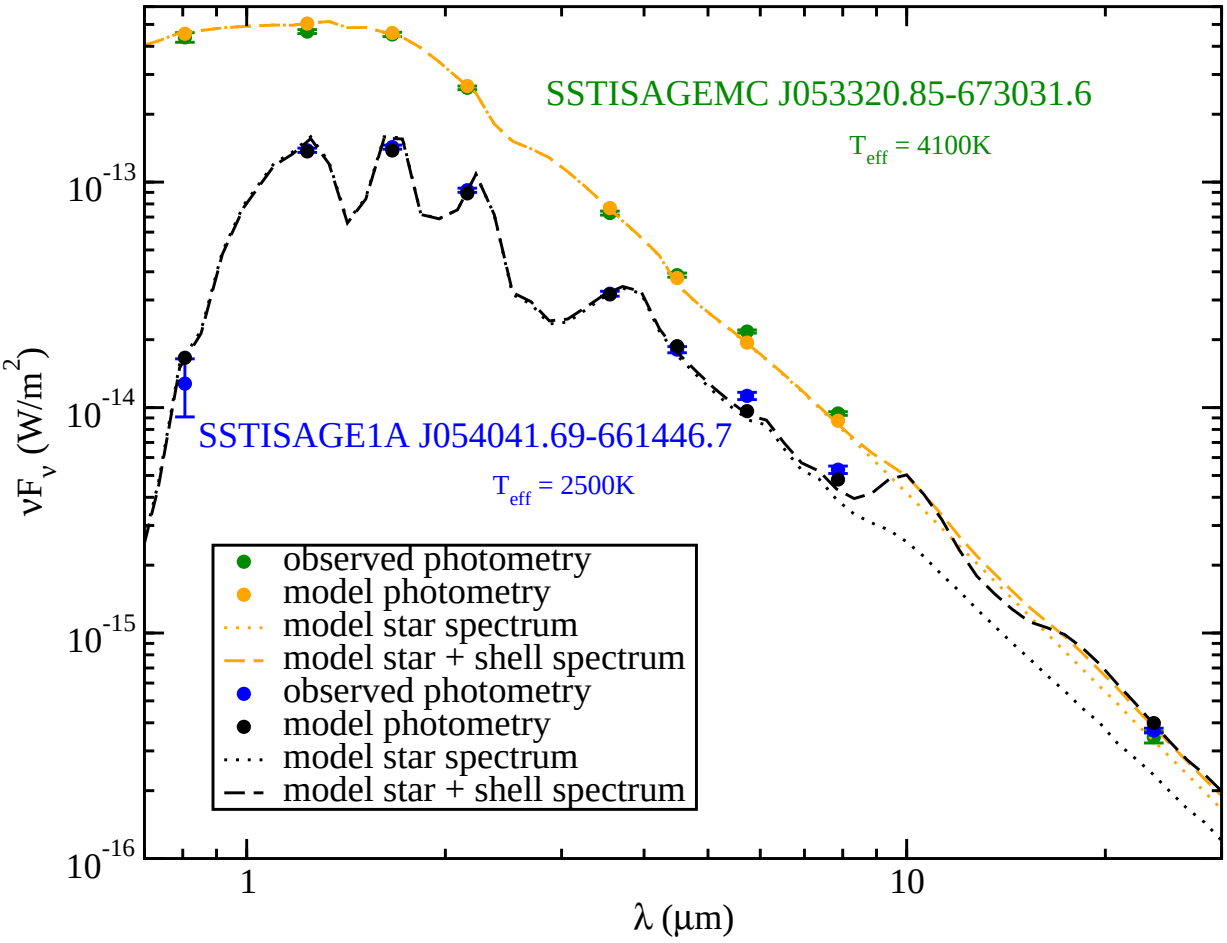

Fig. 11.— Best fit models from O-rich evolved star grid fit to broadband photometry of stars with high and low stellar effective temperatures. Green points are observed photometry for star with high T_{eff}, while orange lines are the best fit model for this star. Similarly, blue points are observed photometry for star with low T_{eff}, and black lines are the best fit model for this star. The same symbol convention as was used for Figure 8 is used here.

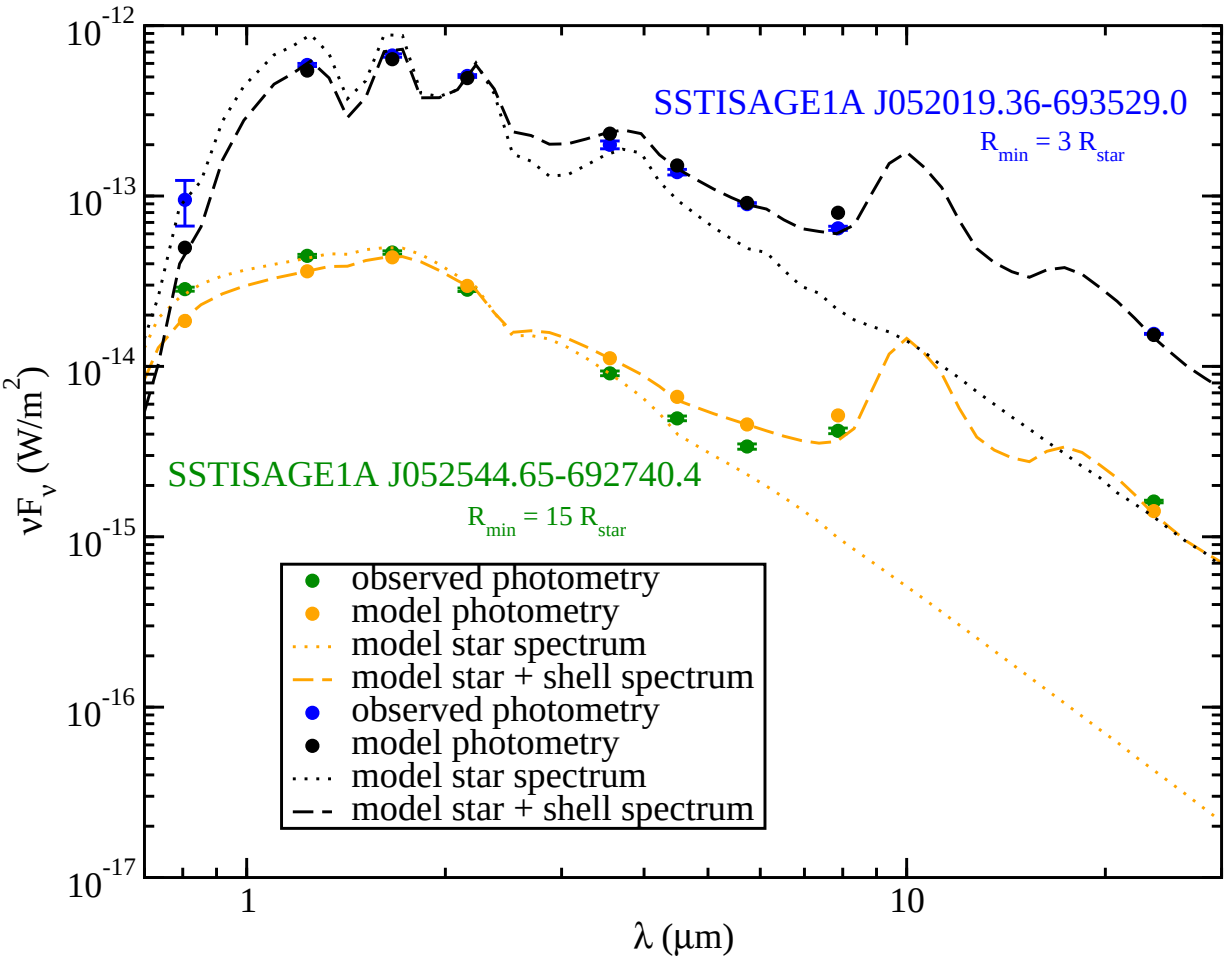

Fig. 12.— Best fit models from O-rich evolved star grid fit to broadband photometry of stars with high and low dust shell inner radii. Green points are observed photometry for star with high R_{min}, while orange lines are the best fit model for this star. Similarly, blue points are observed photometry for star with low R_{min}, and black lines are the best fit model for this star. The same symbol convention as was used for Figure 8 is used here.

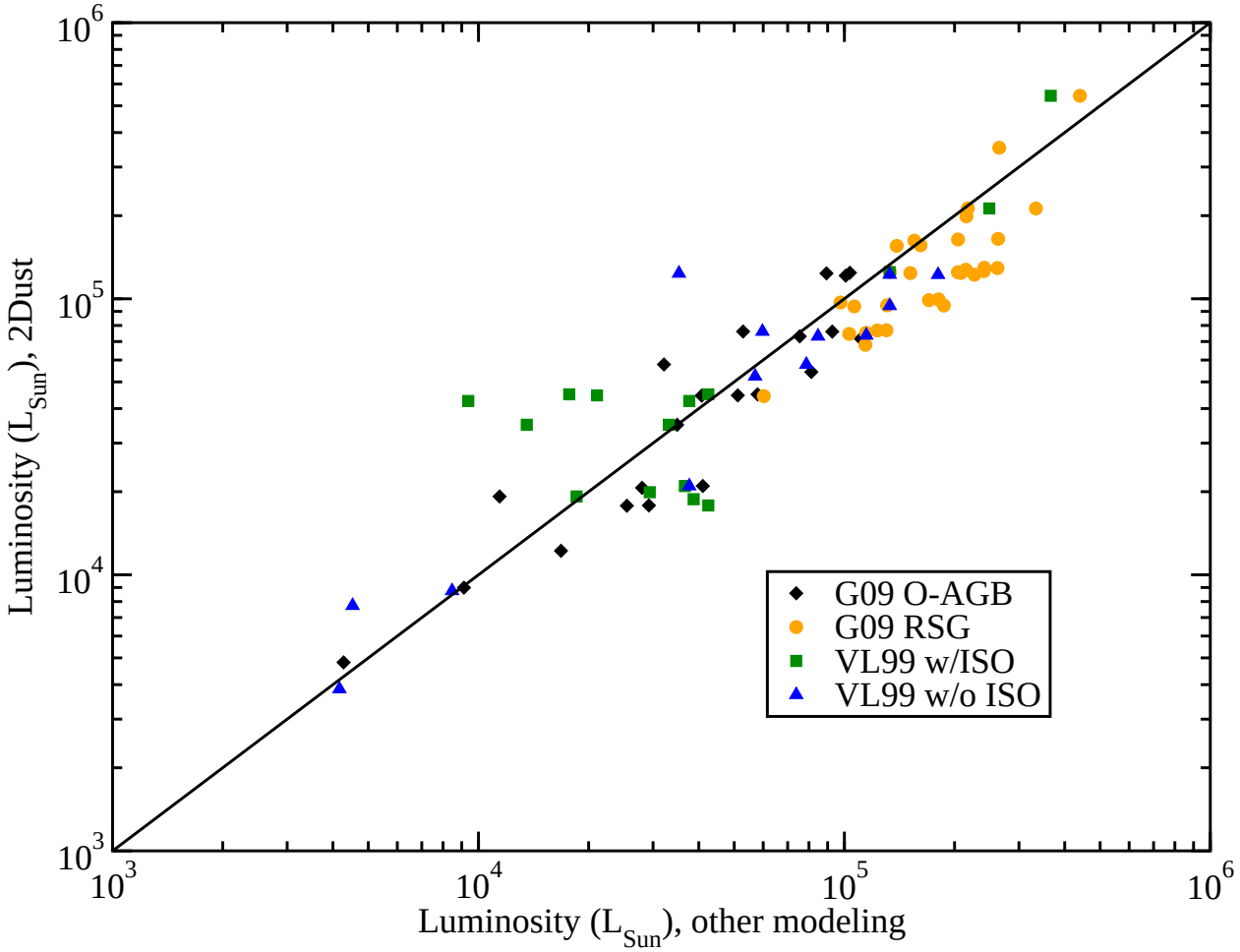

Fig. 13.— A comparison of luminosities obtained from fitting **2D**ust models from the GRAMS grid to SAGE data for stars that were also fit by van Loon et al. (1999) and Groenewegen et al. (2009). Black diamonds are for O-rich AGB stars from the Groenewegen et al. (2009) sample, orange circles are for RSG stars from the Groenewegen et al. (2009) sample, green squares are for M stars from van Loon et al. (1999) that have ISO spectra, and blue triangles are for M stars from van Loon et al. (1999) that do not have ISO spectra. The black diagonal line would represent where points would lie if the luminosities obtained by **2D**ust agreed perfectly with those obtained from the other two modeling studies.

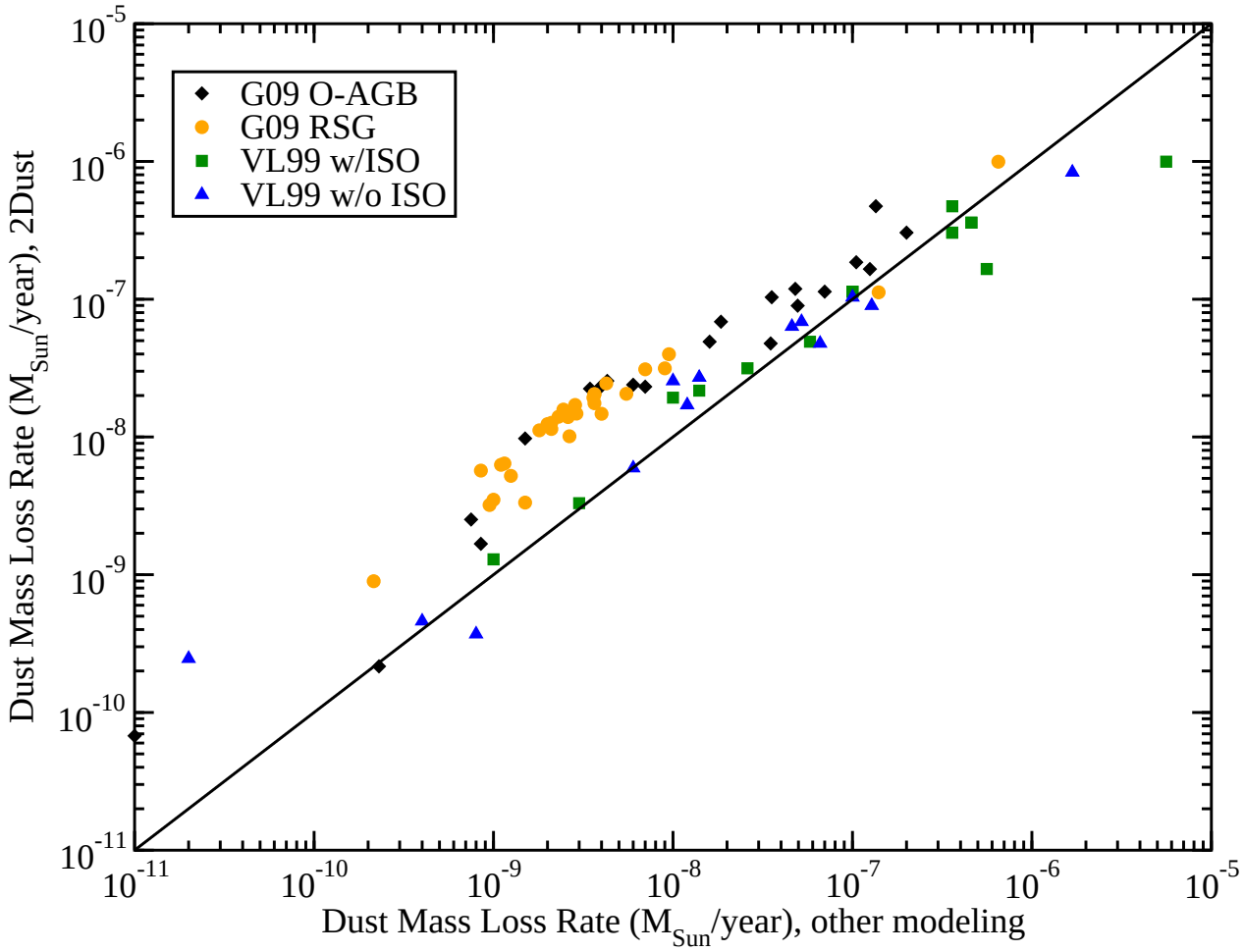

Fig. 14.— A comparison of dust mass-loss rates obtained from fitting **2D**ust models from the GRAMS grid to SAGE data for stars that were also fit by van Loon et al. (1999) and Groenewegen et al. (2009). Total mass-loss rates from the van Loon et al. (1999) and Groenewegen et al. (2009) studies were converted to dust mass-loss rates using the gas-to-dust mass ratios that each reference quotes (500 and 200, respectively). Same symbol convention as for Figure 13, except that the black diagonal line would represent perfect agreement in dust mass-loss rate between **2D**ust modeling and the modeling reported by the other two studies.

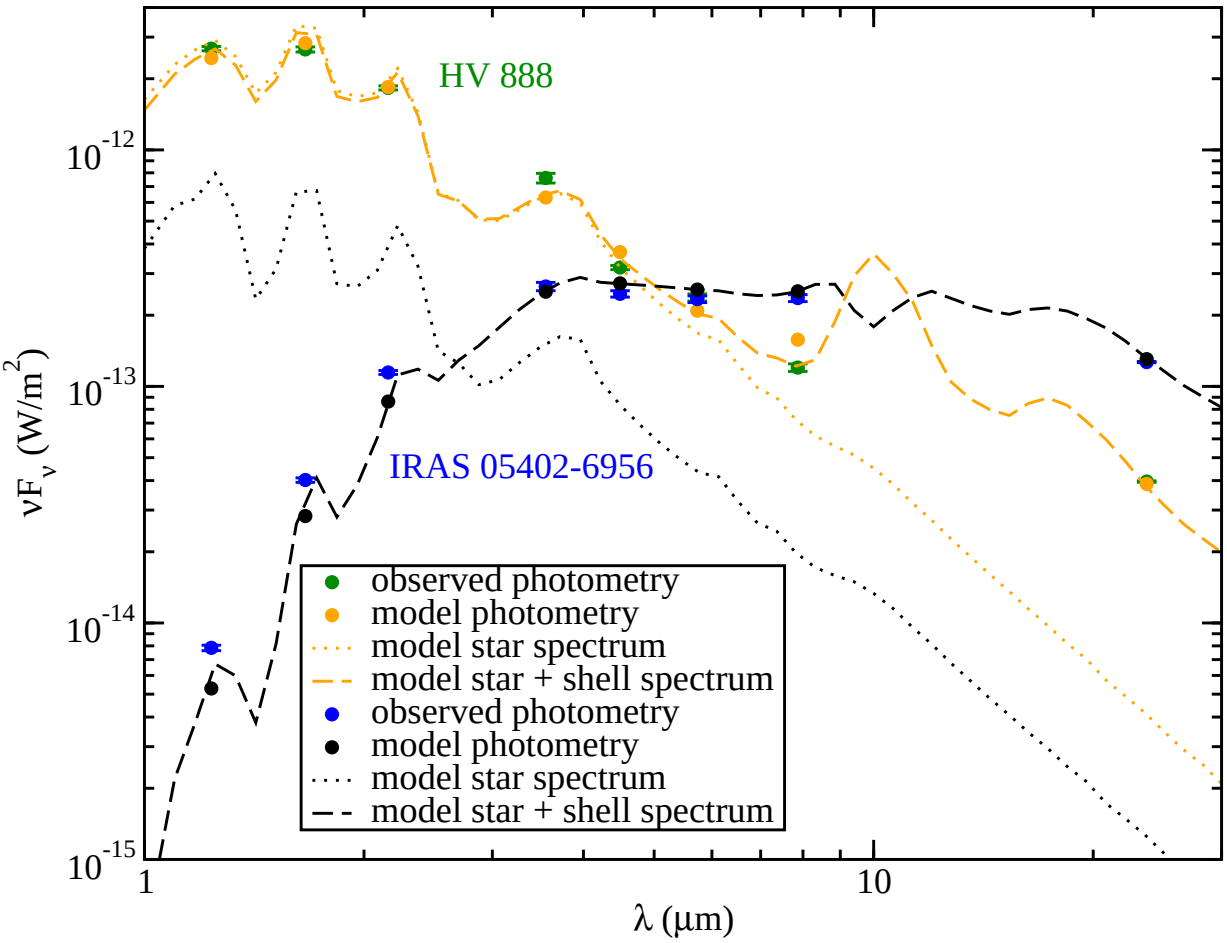

Fig. 15.— Best fit models from O-rich evolved star grid fit to broadband photometry of stars that were also fit by both van Loon et al. (1999) and Groenewegen et al. (2009). Green points are observed photometry for HV 888, while orange lines are the best fit model for this star. Similarly, blue points are observed photometry for IRAS 05402-6956, and black lines are the best fit model for this star. The same symbol convention as was used for Figure 8 is used here.

Table 1: Parameters for Models in Grid

Parameter	Range of Values	Increment
Star		
T_{eff} (K)	2100–4700	+200
Log(g)	-0.5	···
Log(Z/Z_{sun})*	-0.5	···
$L_{star}(L_{\odot})$	10^3–10^6	$\times$1.08, $\times$1.3[a]
Dust Grains		
ρ_{dust} (g/cm^3)*	3.3	···
γ*	-3.5	···
$a_{min}(\mu$m)*	0.01	···
$a_0(\mu$m)*	0.1	···
Assumed Values		
R_{max}/R$_{min}$*	10^3	···
v_{exp} (km/s)*	10	···
Dust Shell		
τ_{10}	10^{-4}–26	$\times$2, +1[b]
$R_{min}(R_{star})$	3, 7, 11, & 15	+4
$\dot{M}_{dust}(M_{\odot}yr^{-1})$	3×10^{-13}–3×10^{-5}	···

Note. — A KMH grain size distribution n(a) $\propto$ a$^{\gamma}$e$^{-a/a_0}$ (Kim et al. 1994) was used for both models. An asterisk (*) indicates a parameter was fixed.

[a]As described in the text, the gridding in luminosity is finer, with multiplicative factors of $\sim$1.08, for luminosities less than $20000L_{\odot}$, than for luminosities greater than this, which have multiplicative factors of $\sim$1.3.

[b]As described in the text, the gridding in τ_{10} is in multiplicative factors of 2 between τ_{10} of 10^{-4} and 0.41, and the gridding in τ_{10} is linear for τ_{10} between 1 and 26, with increments of 1.

Table 2: Comparison of Models

Parameter	SSTSAGE052206 all data[a]	SSTSAGE052206 χ^2-min[b]	HV 5715 all data[a]	HV 5715 χ^2-min[b]
L ($L_\odot$)	5100	4900	36000	33000
τ_{10}	0.095	0.10	0.012	0.026
$\dot{M}_{\rm d}$ ($M_\odot yr^{-1}$)	2.0×10^{-9}	2.1×10^{-9}	2.3×10^{-9}	1.5×10^{-9}

[a]These columns have parameter values that are for the best-fit models from Sargent et al. (2010) for models fit to the *Spitzer*-IRS spectra and all available photometry.

[b]These columns have parameter values that are for the best-fit models found by χ^2-minimization fitting of photometry over 9 bands, as described in §4.2 of this paper.